Chemical Science

ROYAL SOCIETY OF CHEMISTRY

REVIEW

View Article Online
View Journal | View Issue

Cite this: *Chem. Sci.*, 2021, **12**, 14004

Designs and understanding of small molecule-based non-fullerene acceptors for realizing commercially viable organic photovoltaics

Minjun Kim,[b] Seung Un Ryu,[a] Sang Ah Park,[a] Yong-Jin Pu[b] and Taiho Park *[a]

Organic photovoltaics (OPVs) have emerged as a promising next-generation technology with great potential for portable, wearable, and transparent photovoltaic applications. Over the past few decades, remarkable advances have been made in non-fullerene acceptor (NFA)-based OPVs, with their power conversion efficiency exceeding 18%, which is close to the requirements for commercial realization. Novel molecular NFA designs have emerged and evolved in the progress of understanding the physical features of NFA-based OPVs in relation to their high performance, while there is room for further improvement. In this review, the molecular design of representative NFAs is described, and their blend characteristics are assessed *via* statistical comparisons. Meanwhile, the current understanding of photocurrent generation is reviewed along with the significant physical features observed in high-performance NFA-based OPVs, while the challenging issues and the strategic perspectives for the commercialization of OPV technology are also discussed.

Received 19th July 2021
Accepted 7th October 2021

DOI: 10.1039/d1sc03908c

rsc.li/chemical-science

1. Introduction

The photovoltaic (PV) technology for converting sunlight into electricity is one of the sustainable solutions for overcoming the energy crisis and addressing climate change and is a rapidly growing field with increasing efficiencies.[1,2] While various other PV types are being actively developed, organic photovoltaic (OPV) technology is emerging as the next-generation PV technology with great potential for portable, flexible/stretchable, and transparent applications.[3–7] With significant advances in material designs, film processing techniques, and device architectures,[8–12] the power conversion efficiency (PCE) of OPVs has reached around 18%, which is close to the requirements for commercialization.[13–17]

Two major breakthroughs in the history of OPV technology have significantly boosted device efficiency. While early-stage OPV devices adopted a single-component material for the photoactive layer and the PCE was only ~1%, the advent of the bulk-heterojunction (BHJ) system[18–20] blended with an electron

[a]*Department of Chemical Engineering, Pohang University of Science and Technology (POSTECH), 77 Cheongam-ro, Nam-gu, Pohang, Gyeongsangbuk-do, 37673, Republic of Korea. E-mail: taihopark@postech.ac.kr*

[b]*RIKEN Center for Emergent Matter Science (CEMS), 2-1 Hirosawa, Wako, Saitama, 351-0198, Japan. E-mail: minjun.kim@riken.jp; yongjin.pu@riken.jp*

Minjun Kim is a post-doctoral researcher in RIKEN, CEMS, Japan, under the supervision of Dr Yong-Jin Pu since 2019. He received his Ph.D. degree from the Department of Chemical Engineering at POSTECH, South Korea, in 2019, under the supervision of Prof. Taiho Park. His current research interests are the development of organic-based electronic materials and the photophysics of optoelectronic materials.

Taiho Park is a Namgo endowed chair professor of POSTECH. He received his Ph.D. degree from the University of Cambridge, UK, under the supervision of Prof. Andrew B. Holmes in 2003, and then worked as a post-doctoral researcher under Prof. Steven C. Zimmerman at the University of Illinois (Urbana-Champaign), USA. He joined the faculty in the Department of Chemical Engineering at POSTECH in March of 2007. His current research interests include the material properties and device functions of optoelectronic devices.

donor (D) and an acceptor (A) has allowed for improving the PCE by more than 10%, the first significant breakthrough in the OPV field.[21,22] The BHJ system has demonstrated efficient photocurrent generation *via* increasing the D/A interfacial area and is widely adopted in most OPV devices.[18–20] Specifically, the BHJ blend OPVs consisting of a polymer donor and a fullerene acceptor (FA) (*e.g.*, $PC_{61}BM$ and $PC_{71}BM$) have received a great deal of attention, providing a comprehensive understanding of the photo-conversion process in the BHJ blend system as well as valuable insights into the design of high-performance OPVs. The PCE of FA-based binary blend OPVs has reached up to ~12% (ref. 23) through the development of numerous polymer donors (*e.g.*, 11.7% for PffBT4T-C_9C_{13}:$PC_{71}BM$); however, further improvements have been hindered by various critical drawbacks, including narrow and weak light absorption, large voltage loss, and thermal and/or photo-chemical instability.[24–26] Meanwhile, chemically modifiable non-fullerene acceptors (NFAs) have emerged as an alternative to FAs for overcoming the aforementioned optical and photophysical issues.[8,27–35] In practice, employing an NFA as a host acceptor in binary blends[17,24,31,36] or as a secondary acceptor in ternary blends[37–41] has proven to exceed the theoretical efficiency (~15%) of FA-based OPVs,[42] which presents the second major breakthrough in OPV technology. As the molecular design of NFAs continues to evolve, NFA-based binary blend OPVs have recently demonstrated a high PCE of over 18%,[15,17] indicating their potential for meeting the commercial requirements (*e.g.*, 18–22% for silicon solar cells). Moreover, NFA-based OPVs have the technological capacity for wearable and transparent PV applications owing to their excellent mechanical stability[4] and near-infrared (NIR) light absorption.[6,7,43–48]

The distinctive features of NFA-based OPVs become clear following statistical comparisons with FA-based OPVs (Fig. 1). One significant feature of NFA-based OPVs is the high short-circuit current density (J_{SC}) with a small optical bandgap (E_g), *i.e.*, the smaller optical bandgap of the donor or acceptor (Fig. 1a and b). In fact, FA-based OPVs have a E_g distribution concentrated at 1.5–1.8 eV, with the J_{SC} being less than 20 mA cm^{-2}. Meanwhile, in terms of NFA-based OPVs, the E_g is mainly distributed in the 1.2–1.6 eV range, while they exhibit a higher J_{SC} (>20 mA cm^{-2}) than FA-based OPVs at E_g < 1.5 eV. The other important feature is the low voltage loss (V_{loss}) with a small energy offset (Fig. 1c–f), where the energy offset defines the lowest unoccupied molecular orbital (LUMO) offset (ΔE_{LUMO}) or the highest occupied molecular orbital (HOMO) offset (ΔE_{HOMO}). Here, while FA-based OPVs have a V_{loss} of 0.6–1.2 V at a ΔE_{HOMO} or ΔE_{LUMO} of <1.0 eV, NFA-based OPVs exhibit a lower V_{loss} (<0.8 V) in the same offset region. In fact, comparatively low

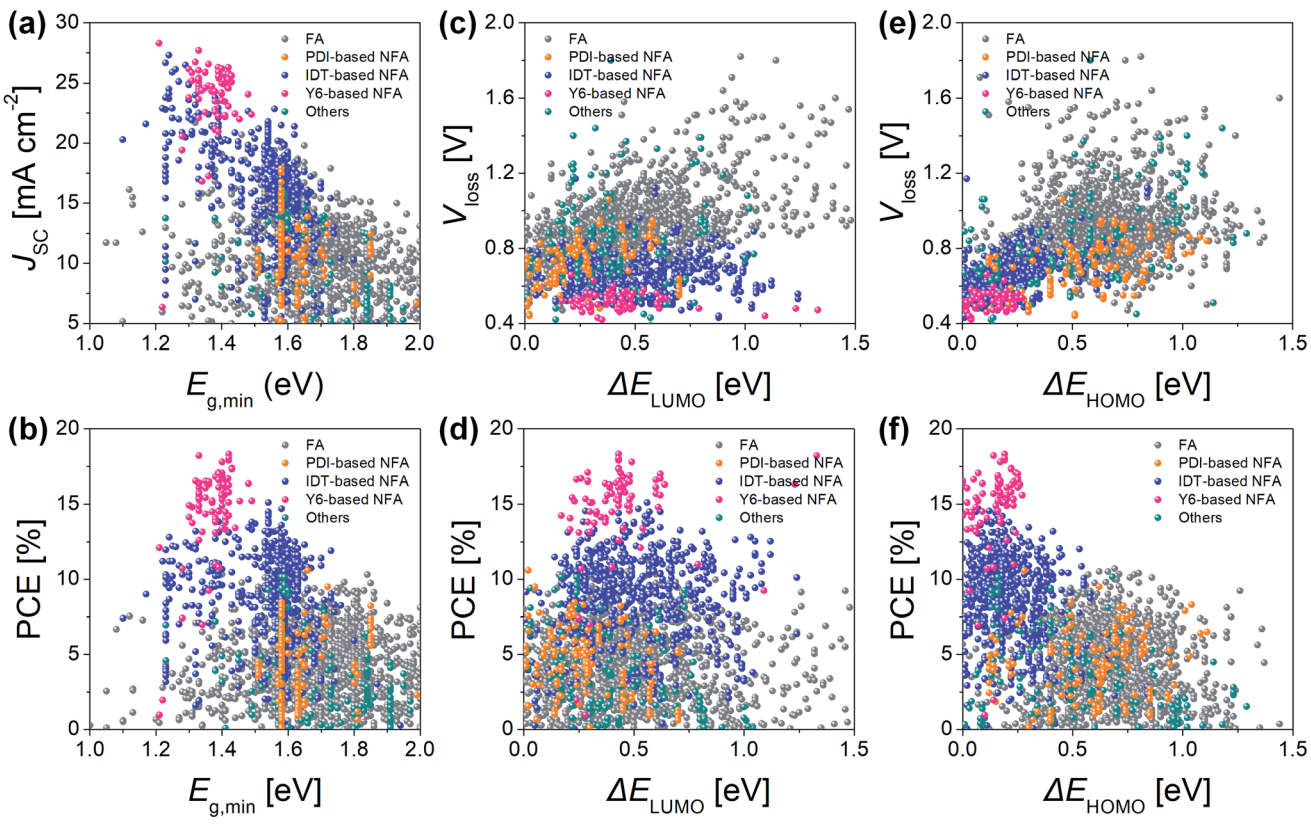

Fig. 1 Statistical data collected from ≈2000 pairs of FA- and NFA-based binary blend OPVs over the last 10 years. (a) Short-circuit current density (J_{SC}) and (b) power conversion efficiency (PCE) *versus* $E_{g,min}$. (c) Voltage loss (V_{loss}) and (d) PCE *versus* the lowest unoccupied molecular orbital (LUMO) offset (ΔE_{LUMO}). (e) V_{loss} and (f) PCE *versus* the highest occupied molecular orbital (HOMO) offset (ΔE_{HOMO}). The each color means data of polymer donor:FA (grey dots), polymer donor:PDI-based NFA (orange dots), polymer donor:IDT-based NFA (navy dots), polymer donor:Y6-based NFA (pink dots) and polymer donor:others (NFAs which are not included in PDI, IDT, and Y6 categories) (green dots).

V_{loss} ($\approx$0.5 V) values can be observed in many NFA-based OPVs with a ΔE_{HOMO} of <0.3 eV. These statistical comparisons indicate that NFA-based OPVs generate a photocurrent with different operating mechanisms compared with FA-based OPVs; however, the origin of the significant improvements in the performance of NFA-based OPVs has, as yet, not been fully understood. In addition to the features of E_g and energy offset (*i.e.*, ΔE_{LUMO} and ΔE_{HOMO}), various updated materials and physical discoveries related to NFA-based OPVs are being regularly reported, thus providing a better fundamental understanding for designing high-performance OPVs.

In this review, we first cover the existing knowledge regarding the operating principles of OPVs (Section 2) and describe the molecular designs of representative NFAs in relation to the statistically collected PV parameters (Section 3). Following this, we review the current understanding and the significant features observed in NFA-based OPVs, with a specific focus on the photophysical, electrical, and morphological characteristics (Section 4). Finally, we provide a concise summary and discuss the various perspectives on realizing high-performance and functional OPVs for technological commercialization (Section 5).

2. OPV operation

The OPV operation involves photocurrent generation *via* a sequential process in the BHJ active layer (Fig. 2),[20,26,49,50] which consists of the following stages: (1) Frenkel excitons (*i.e.*, tightly bound electron–hole pairs) are formed following light absorption, (2) the excitons diffuse to the D/A interfaces and form charge transfer (CT) excitons (*i.e.*, weakly bound electron–hole pairs), (3) the CT excitons are dissociated into free charge carriers by the built-in potential in devices, (4) the free charges transport to each electrode (*i.e.*, holes to anode, electrons to cathode), and (5) the charges are collected at the electrodes, thus generating an electric current. The overall efficiency (η) of photocurrent generation is defined as follows:

$$\eta = \eta_{abs}\eta_{ed}\eta_{CT}\eta_{CC} \quad (1)$$

where η_{abs}, η_{ed}, η_{CT}, and η_{CC} are the efficiency of photon absorption, exciton diffusion, CT exciton dissociation, and charge collection, respectively. Here, η_{abs} is affected by the range and intensity of the light absorption, while η_{CT} is highly associated with the energy offset between E_g and the energy of the CT state (E_{CT}). Meanwhile, the η_{ed} and η_{CC} are greatly influenced by the blend morphology and charge carrier mobility of the materials.

In practice, the PV characteristics of OPVs are evaluated in terms of current–voltage (*I–V*) measurements, where the output current is obtained at each step of an applied voltage under solar illumination. The efficiency in converting sunlight to electricity (*i.e.*, PCE) is estimated from the measured *I–V* curve and is defined as follows:[51,52]

$$PCE = \frac{J_{SC} \times V_{OC} \times FF}{P_{in}} \quad (2)$$

where P_{in} is the intensity of the incident sunlight under AM 1.5G (P_{in} = 100 mW cm^{-2} at the AM 1.5G condition) and J_{SC}, open-circuit voltage (V_{OC}), and fill factor (FF) are the main PV parameters for determining the PCE of the device. The parameters J_{SC}, V_{OC}, and FF are closely related to each other and are influenced by various factors, including the material, the blend system, the morphology, and the device architecture. As such, the underlying origin of the three parameters has not yet been fully established, and numerous relevant studies are actively underway (see Section 4).

3. Molecular designs of NFAs

Among the various NFAs, three types of molecular design, perylenediimide (PDI)-based, indacenodithiophene (IDT)-based, and Y6-based, have demonstrated outstanding PV performances (see Fig. 1).[32,36,53] In this section, we describe the molecular design for these three types of NFA in terms of the optoelectronic and structural properties required for high-performance OPVs, while the device characteristics observed in various blend systems are also discussed (the chemical structures of polymer donors, FAs, PDI-based NFAs, IDT-based NFAs, and Y6-based NFAs are shown in Fig. 3, and OPV performance of representative FA- and NFA-based OPVs is shown in Table 1).

3.1. PDI-based NFAs

The PDI unit has a large planar structure with tetracarboxylic diimide groups, which means PDI-based molecules have strong

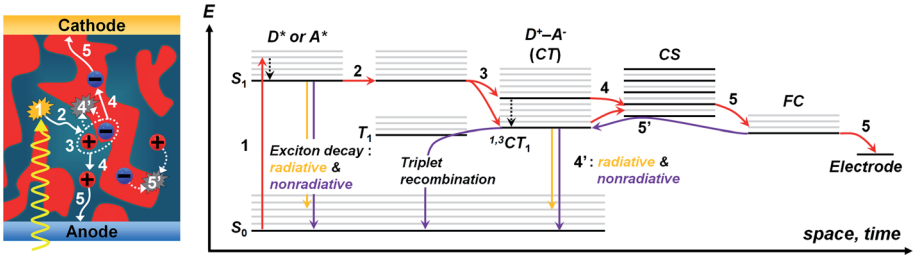

Fig. 2 Illustration of OPV operation according to a sequential process: (1) light absorption and exciton generation, (2) exciton diffusion, (3) charge separation, (4) charge transport, (4′) geminate recombination, (5) charge collection, (5′) non-geminate recombination (left), excited-state Jablonski diagram for description of charge generation and recombination processes in OPVs based on the BHJ active layer (S_0: ground state; S_1: the lowest singlet state; T_1: the lowest triplet state; CT: charge transfer state; CS: charge separation state; FC: free charge carrier) (right).

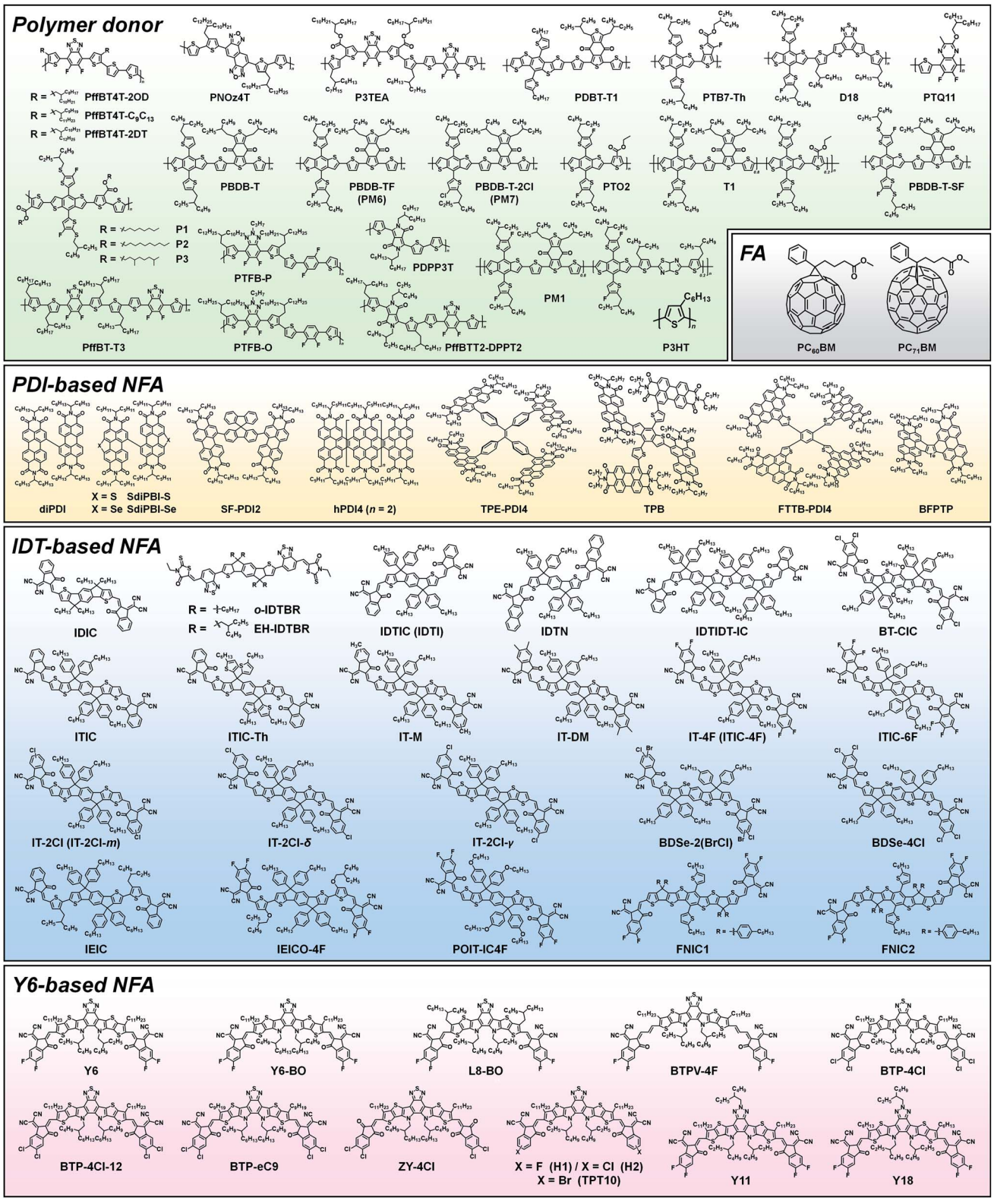

Fig. 3 Chemical structures of polymer donors, FAs, and NFAs (PDI-based NFA, IDT-based NFA, and Y6-based NFA) discussed in this review.

intermolecular interaction and high electron affinity (LUMO ≈ −3.8 eV).[32,54] Hence, PDI-based molecules are currently employed as electron-accepting[54–57] and/or transporting materials[57–60] in organic electronic devices. However, the self-aggregation induced by the strong intermolecular interactions among the PDI units lowers the solubility in common solvents and forms particularly large domains in BHJ blends, thus limiting the exciton dissociation and diffusion.[32,61,62] The

Table 1 OPV performance of representative polymer donor:FA and polymer donor:NFA blend photoactive layers

Acceptor	Donor	V_{OC} [V]	J_{SC} [mA cm^{-2}]	FF [%]	PCE [%]	V_{loss} [V]	Ref.
FAs							
$PC_{71}BM$	PffBT4T-C_9C_{13}	0.78	19.8	73	11.7	0.87	23
$PC_{71}BM$	PffBT4T-2OD	0.77	18.4	74	10.5	0.88	22
$PC_{71}BM$	PNOz4T	0.96	14.5	64	8.9	0.56	74
PDI-based NFAs							
SdiPBI-S	PDBT-T1	0.90	11.7	66	7.2	0.95	66
SdiPBI-Se	PDBT-T1	0.95	12.5	70	8.4	0.90	67
SF-PDI2	P3TEA	1.11	13.3	64	9.5	0.61	69
hPDI4	PTB7-Th	0.80	15.2	68	8.3	0.78	64
TPB	PTB7-Th	0.79	17.9	58	8.5	0.79	70
FTTB-PDI4	P3TEA	1.13	13.9	66	10.6	0.53	72
IDT-based NFAs							
IT-4F	T1	0.90	21.5	78	15.1	0.64	75
IT-4F	PTO2	0.91	21.5	75	14.7	0.67	76
IT-4F	PBDB-T-SF	0.88	20.9	71	13.1	0.66	77
BDSe-4Cl	PM7	0.83	22.5	74	13.8	0.56	78
BDSe-2(BrCl)	PM7	0.83	22.9	77	14.5	0.56	78
POIT-IC4F	PM6	0.91	20.9	73	13.8	0.58	79
Y6-based NFAs							
Y6	D18	0.86	27.7	77	18.2	0.47	15
Y6-BO	PM6	0.86	25.3	76	16.4	0.48	80
L8-BO	PM6	0.87	25.7	82	18.3	0.55	17
BTP-4Cl-12	PM6	0.86	25.6	78	17.0	0.53	81
BTP-eC9	PM6	0.84	26.2	81	17.8	0.56	16
Y11	PM6	0.83	26.7	74	16.5	0.48	82

molecular design of PDI-based materials appears to suppress the self-aggregation through structural torsion[63] or ring fusion.[64] Here, the structure of PDI dimers or tetramers linked through C–C single bonds[65–67] or π-conjugated units[68–71] (*e.g.*, spirofluorene and benzene) exhibit highly twisted conformation with torsional angles of 40°–80°, which effectively inhibits the self-aggregation in blend films. Nonetheless, low device performance remains an issue in twisted PDI-based blend OPVs because of their low electron mobility (μ_e) and narrow light absorption (400–600 nm). Here, the ring fusion of PDI-based NFAs can lower the torsional angles between the units ($\approx 25°$),[64] resulting in closer intermolecular packing than that in PDI dimers and tetramers. These structural features have been reported to be effective in improving the μ_e ($\approx 10^{-3}$ cm^2 V^{-1} s^{-1}) without generating large domains in blend films. For example, ring fusion to PDI tetramer (FTTB-PDI4)[72,73] builds a "double-decker" geometry, where adjacent PDI units exhibit close to parallel conformation for close intermolecular packing.

The high-performance blend system of PDI-based NFAs and polymer donors ($E_g \approx 1.6$ eV) exhibits a light absorption in the 300–800 nm range and a J_{SC} of 15–20 mA cm^{-2}, which is similar to FA-based OPVs (Fig. 1a). Meanwhile, the V_{loss} of PDI-based OPVs is mainly distributed in the 0.6–0.8 V range at a ΔE_{LUMO} of <0.5 eV, and is around 0.4 V smaller than that of FA-based OPVs (Fig. 1c).

3.2. IDT-based NFAs

The IDT unit, a pentacyclic ladder-type arene, has a five-fused aromatic structure with high planarity and strong rigidity.[83,84] The introduction of IDT as a core unit in organic semiconductors (*e.g.*, small molecules or polymers) enhances the intermolecular interaction and structural resilience, demonstrating high charge carrier mobility with a low degree of energetic disorder.[85] Most IDT-based NFAs adopt the A–D–A type structure, with two strong electron-withdrawing end-groups (*e.g.*, indanone or rhodanine derivatives) attached to the IDT core unit. The A–D–A structure in IDT-based NFAs effectively reduces the E_g to a great extent through efficient intramolecular charge transfer (ICT), providing NIR light absorption with an onset of 800–1100 nm ($E_g = 1.2$–1.6 eV). In addition, IDT-based NFAs have low crystallinity, exhibiting a well-mixed blend morphology with polymer donors.[86–88]

The molecular design of IDT-based NFAs has evolved through chemical modifications of the backbone, side chains, and end-groups.[32,89] Increasing the number of fused rings or inserting additional electron-donating units has proven to be effective in reducing the E_g of IDT-based NFAs through extending the conjugation length.[44,90–92] The bulky side chains on the sp^3-hybridized carbon (C) atoms of the IDT unit play an important role in determining the solubility of IDT-based NFAs, but cause some steric hindrance among the IDT units. Hence, for the most part, IDT-based NFAs have a linear stacked packing structure formed through end-group π–π stacking,[36,93] and the modification of the alkyl side chains (*e.g.*, shape, length, and branch position) has been exploited to modulate the intermolecular interactions and the blend miscibility with the polymer donors.[94,95] Chemically substituting hydrogen (H) atoms of the

end-group with strong electronegative atoms (*e.g.*, fluorine [F] and chlorine [Cl]) has also proven to be an effective molecular design strategy for improving the μ_e ($\approx 10^{-4}$ cm^2 V^{-1} s^{-1}) of IDT-based NFAs through enhancing the intermolecular interactions.[77,96–98]

The blend system of IDT-based NFAs and polymer donors (*e.g.*, PBDB-T analogs, PTB7-Th) covers the light absorption in the range of 400–1000 nm, and IDT-based devices with an E_g of <1.5 eV tend to exhibit a high J_{SC} of >20 mA cm^{-2} (Fig. 1a). Specifically, the PTB7-Th:IEICO-4F device[99] achieves the highest J_{SC} of 27.3 mA cm^{-2} among all the IDT-based blend OPVs. The V_{loss} of IDT-based blends tends to be sensitive to the ΔE_{HOMO} and has a narrow distribution of 0.4–0.8 V at a ΔE_{HOMO} of <0.5 eV (Fig. 1e).

3.3. Y6-based NFAs

Unlike IDT-based NFAs, the molecular design feature of Y6-based NFAs revolves around the adoption of an electron-deficient polycyclic arene as a core unit, in which benzothiadiazole and dithienothiophene[3,2-*b*]-pyrrolo are fused (*i.e.*, D–A′–D-type structure).[7,100–102] With two end-groups linked to the core unit (*i.e.*, A–D–A′–D–A structure), Y6-based NFAs exhibit a crescent shape and an axisymmetric structure.[100,101] The A–D–A′–D–A structure in Y6-based NFAs enables a smaller E_g (1.2–1.4 eV) than do IDT-based NFAs through a strong ICT effect, absorbing light with an onset of 900–1100 nm. Another feature of Y6-based NFAs is the multiple packing between the core units or end-groups,[103,104] since the alkyl side chains are attached to the sp^2-hybridized nitrogen (N) atoms of the core unit, less bulky than the sp^3-hybridized C atoms (*i.e.*, one alkyl chain per N atom and two alkyl chains per C atom). The multiple packing results in the efficient electron transport of Y6-based NFAs with a μ_e of $\approx 10^{-4}$ cm^2 V^{-1} s^{-1}.[101,103,104]

Similar to IDT-based NFAs, the molecular modification of Y6-based NFAs has been focused on the electronic and structure properties. The extension of the fused-ring core and the insertion of a π-linker have been the main approaches in terms of backbone modification in view of increasing the effective conjugation length of Y6-based NFAs (*i.e.*, smaller E_g),[105–107] while modifications of the alkyl side chains have also been employed to control the intermolecular packing and solubility in this type of NFA.[16,17,80,108] Interestingly, it has recently been demonstrated that the alkyl side chains adjacent to the end-groups prevent the rotating end-groups (*i.e.*, conformational locking), thereby lowering the energetic disorders to improve the charge transport.[109,110] Meanwhile, the end-group of Y6-based NFAs has largely been modified through chemical substitutions using electronegative atoms (*e.g.*, F and Cl) to control the LUMO levels and molecular packing, much like in IDT-based NFAs.[101,111,112]

The Y6-based blend system exhibits a complementary light absorption of 400–1100 nm with polymer donors (*e.g.*, PBDB-T analogs or PTB7-Th). The Y6-based devices with an E_g of <1.4 eV attain a high J_{SC} of >23 mA cm^{-2} (Fig. 1a). The V_{loss} of the Y6-based blends is distributed in the 0.4–0.6 V range with an average of 0.52 V at a ΔE_{HOMO} of <0.3 eV, which is much lower than those of the other two types of NFA-based OPV (Fig. 1e). A significant number of Y6-based blends have exhibited excellent device performance, with a PCE of 15–18%, while most recently, the highest PCE of 18.32% has been reported in a Y6 analog-based device (PBDB-TF:L8-BO).[17]

4. Key physical features in NFA-based OPVs

The increase in the J_{SC} and V_{OC} of NFA-based OPVs can be largely attributed to the specific molecular design of the NFA, which creates distinctive physical features that differ from those of FA-based OPVs. In this section, we describe the physical features observed in NFA-based OPVs in relation to those of FA-based OPVs and review the current understanding of their fundamental aspects in terms of light harvesting, voltage loss, charge transport, triplet-exciton utilization, and blend morphology.

4.1. Light harvesting

4.1.1. Photon absorption. The degree of conversion from sunlight (*i.e.*, incident photon) to electrical current is described in terms of the external quantum efficiency (EQE), which is defined as follows:[49]

$$\mathrm{EQE} = \eta_{abs}\mathrm{IQE} \tag{3}$$

The internal quantum efficiency (IQE) is the ratio of the number of charge carriers collected by the device to the number of photons from the device (*i.e.*, photons absorbed by the device). The J_{SC}, one of the main PV parameters, is expressed as follows:[49]

$$J_{SC} = q\int_{E_g}^{\infty} \mathrm{EQE}(E)\varnothing_{AM1.5G}(E)\mathrm{d}E \tag{4}$$

where q, E, and $\varnothing_{AM1.5G}$ are the elementary charge, photon energy, and air mass (AM) 1.5G solar spectrum, respectively. The EQE(E) under the Shockley–Queisser (SQ) limit is expressed as an ideal step-like function:[49,113]

$$\mathrm{EQE} = \begin{bmatrix} 100\% & E \geq E_g \\ 0 & E < E_g \end{bmatrix} \tag{5}$$

In theory, when photons with $E \geq E_g$ are absorbed, they are completely converted to electricity, and the J_{SC} can be maximized to $J_{SC,SQ}$ (Fig. 4a).

$$J_{SC,SQ} = q\int_{E_g}^{\infty} \varnothing_{AM1.5G}(E)\mathrm{d}E \tag{6}$$

In addition, the solar irradiance in the range of 400–800 nm is over 1.0 W m^{-2} nm^{-1} (Fig. 4b), indicating that a large number of photons are provided in this region. Therefore, a desirable D/A blend should have a strong absorption coefficient (α) while absorbing visible and NIR regions (>400 nm).

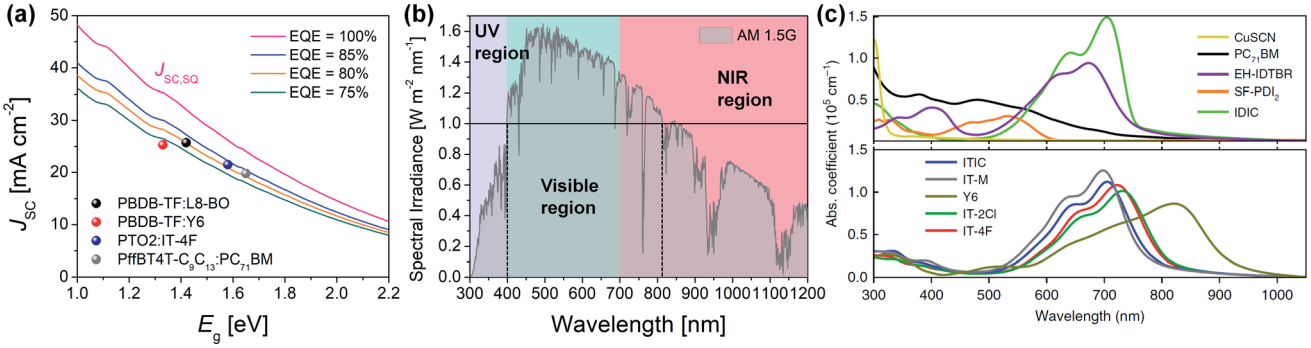

Fig. 4 (a) Calculated J_{SC} as a function of E_g according to the external quantum efficiency (EQE) assumed to be a constant value above the E_g. J_{SC} of representative FA- and NFA-based OPVs (*i.e.*, PBDB-TF:L8-BO,[17] PBDB-TF:Y6,[101] PTO2:IT-4F,[76] and PffBT4T-C_9C_{13}:$PC_{71}BM$[23]). (b) Solar spectrum under AM 1.5G; purple (≤400 nm), green (400–700 nm), and red (≥700 nm) area mean UV, visible, and near-infrared (NIR) region, respectively. Black solid line represents spectral irradiance of 1.0 W m^{-2} nm^{-1} and black dotted lines provide the region over spectral irradiance of 1.0 W m^{-2} nm^{-1} (400–800 nm). (c) Absorption coefficient (α) of $PC_{71}BM$ and NFAs (EH-IDTBR, SF-PDI2, IDIC, ITIC, IT-M, Y6, IT-2Cl, and IT-4F). Reproduced with permission.[116] Copyright 2020, Springer Nature.

Conventional FAs (*e.g.*, $PC_{61}BM$ or $PC_{71}BM$) exhibit a relatively short absorption range of 300–500 nm with weak α values;[114] hence, the light harvesting of FA-based OPVs is largely determined by the absorption of polymer donors. For example, the PffBT4T-C_9C_{13}:$PC_{71}BM$ blend OPV absorbs up to 750 nm of light and exhibits a J_{SC} of 19.8 mA cm^{-2}.[23] Meanwhile, the complementary absorption of medium-E_g polymer donors and narrow-E_g NFAs covers a wide range of light absorption, enabling a high J_{SC} of >20 mA cm^{-2}. This is also related to the extinction coefficient (k), an optical constant for how strongly a material absorbs light at a specific wavelength ($\alpha = 4\pi k/\lambda$, λ is wavelength).[115] Most NFAs have higher α and k values ($\alpha > 1.0 \times 10^5$ cm^{-1}; $k > 1.0$) than $PC_{71}BM$ ($\alpha \approx 0.9 \times 10^5$ cm^{-1}; $k \approx 0.4$) in the region from visible to NIR (Fig. 4c).[115,116]

The approach to designing D–A-type conjugated molecules is effective in terms of adjusting the E_g *via* the ICT effect and provides variable light absorption. Furthermore, the more planar the molecular backbone, the stronger the ICT effect. In recent years, it has been demonstrated that the molecular design of an A–D–A-type NFA is effective in terms of NIR light absorption because of its high planarity and the strong electron-withdrawing ability of the A units (*e.g.*, E_g = 1.59, 1.51, and 1.24 eV for ITIC, IT-4F, and IEICO-4F, respectively).[77,117–119] The crescent-shaped A–D–A′–D–A-type structure (Y6 analogs) has also demonstrated an effective design approach to NIR light absorption >900 nm (*e.g.*, E_g = 1.33 eV for Y6 and E_g = 1.21 eV for BTPV-4F),[101,107] while devices with Y6 analogs exhibit a high J_{SC} of >23 mA cm^{-2}, which is comparable to that of perovskite solar cells (*e.g.*, 27.7 mA cm^{-2} for D18:Y6 (ref. 15) and 28.3 mA cm^{-2} for PTB7-Th:BTPV-4F[107]).

4.1.2. Exciton diffusion. The photoactive layer thickness is another important factor in efficient light harvesting.[120,121] The photogenerated excitons diffuse to the D/A interface before decaying to a ground state; however, polymer donors and FAs typically have a short exciton diffusion length (L_D) of 5–20 nm,[122,123] which limits the thick-film fabrication of >100 nm with a high J_{SC}. Here, NFA-based OPVs exploit two photocurrent generation channels, exciton generation from the donor (channel-I) and the acceptor (channel-II), while FA-based OPVs operate predominantly on channel-I.[20] Therefore, NFAs with a long L_Ds can greatly improve the photocurrent generation through channel-II.[124,125] Firdaus *et al.* performed EQE measurement of CuSCN/NFA (60–100 nm) bilayer devices and found that representative NFAs (*i.e.*, SF-PDI2, EH-IDTBR, IDIC, ITIC, IT-M, IT-2Cl, IT-4F, and Y6) have a longer L_Ds (20–47 nm) than typical polymer donors and FAs.[116] Subsequently, the exciton annihilation analysis using ultrafast transient spectroscopy revealed that NFAs have higher diffusion coefficients (D) than $PC_{71}BM$ (*e.g.*, D = 0.064 cm^2 s^{-1} for IT-4F and D = 0.00016 cm^2 s^{-1} for $PC_{71}BM$). Meanwhile, quantum chemical calculations for NFAs have revealed that planar and stiff conjugated A–D–A (or A–D–A′–D–A) structures form close molecular packing and reduce the energetic disorder, resulting in a long L_Ds. Recently, Ma *et al.* reported a ~1 μm thick active layer device (PBDB-TF:BTP-4Cl-12) with a high J_{SC} of 27.3 mA cm^{-2}.[126]

4.2. Voltage loss

4.2.1. Energy loss in the CT state. The excitons in organic materials (*i.e.*, Frenkel excitons) have a large binding energy (E_b) of 0.2–1.5 eV because of their low permittivity ($\varepsilon_r \approx$ 3–4).[127] However, the CT excitons at the D/A interface have a lower E_b of 0.3–0.5 eV,[128,129] promoting efficient exciton dissociation into free charges. The E_{CT} is given by the following:[129]

$$E_{CT} = |HOMO_D - LUMO_A| - E_b \quad (7)$$

where $HOMO_D$ is the HOMO of the donor and $LUMO_A$ is the LUMO of the acceptor. Despite the benefits of exciton splitting, CT excitons are the source of substantial V_{loss}. Here, the V_{loss} can be expressed as follows:[130]

$$\begin{aligned} V_{loss} &= E_g/q - V_{OC} \\ &= (E_g/q - E_{CT}/q) + (E_{CT}/q - V_{OC}) \\ &= \Delta E_{CT}/q + \Delta V_{rec} \end{aligned} \quad (8)$$

where ΔE_{CT} ($\Delta E_{CT} = E_g - E_{CT}$) and ΔV_{rec} are the energy offset and the V_{loss} incurred *via* recombination, respectively, which are prominently observed in blend OPVs. While the ΔE_{CT} is the driving force for charge-separation, it presents an inevitable V_{loss} because the E_{CT} lies below the lowest excited state (S_1) of the donor or acceptor. Thus, the ΔE_{CT} should be as small as possible to minimize the V_{loss}. Meanwhile, the ΔV_{rec} term can be divided into radiative recombination (ΔV_{OC}^{rad}) and non-radiative recombination ($\Delta V_{OC}^{non\text{-}rad}$). Most blend OPVs exhibit low luminescence and possess a large $\Delta V_{OC}^{non\text{-}rad}$ (0.4–0.5 eV).[130–132] Therefore, $\Delta V_{OC}^{non\text{-}rad}$ is the main loss in ΔV_{rec} and can be expressed as follows:[129,130,132]

$$\Delta V_{OC}^{non\text{-}rad} = -\frac{k_b T}{q} \ln(EQE_{EL}) \approx -\frac{k_b T}{q} \ln\left(\frac{k_r}{k_r + k_{nr}}\right) \quad (9)$$

where k_b, T, EQE_{EL}, k_r, and k_{nr} are the Boltzmann constant, the temperature, the EQE of electroluminescence (EL), the radiative recombination rate, and the non-radiative recombination rate, respectively. Since the CT rate (k_{CT}) competes with the non-radiative recombination channel (k_{nr}), a higher k_{CT} is desirable to suppress the $\Delta V_{OC}^{non\text{-}rad}$.

4.2.2. Energy offset (ΔE_{CT}). Understanding the physical relationship between the ΔE_{CT} and the k_{CT} can help in determining the optimal ΔE_{CT} in BHJ blends. Here, Coffey *et al.* investigated the k_{CT} and ΔE_{CT} for polymer donor:FA blends and found that the maximum k_{CT} was yielded at an ΔE_{CT} of 0.4–0.8 eV.[133] Elsewhere, Liu *et al.* reported that polymer donor:NFA blends exhibited the maximum k_{CT} even at a low ΔE_{CT} ($\approx$0.2 eV).[134] Meanwhile, various theoretical studies based on the Marcus–Jortner electron transfer theory have described how a low intramolecular (λ_I) and intermolecular reorganization energy (λ_O) can yield a maximum k_{CT} even with a small ΔE_{CT} (Fig. 5a).[129,134]

In terms of molecular structure, increasing the planarity and/or the effective conjugation length of the molecular backbone has proven to be effective in reducing the λ_I. Most NFAs have a lower λ_I (*e.g.*, λ_I = 0.179, 0.101, and 0.157 for IDT-IC, IDTIDT-IC, and BT-CIC, respectively) than FAs (*e.g.*, λ_I = 0.180 for $PC_{71}BM$).[134] The molecular reorientation (*i.e.*, intermolecular reorganization) occurs at the D/A interface during the CT process, changing the charge distribution of the donor and the acceptor. In this regard, the electronic polarization, or the dielectric response, influences the λ_O in CT exciton splitting, which can be simplified in terms of the spherical cavity model established by Marcus:[134–136]

$$\lambda_O = \frac{e^2}{4\pi\varepsilon_0}\left(\frac{1}{\varepsilon_{opt}} - \frac{1}{\varepsilon_r}\right)\left(\frac{1}{2r_D} + \frac{1}{2r_A} - \frac{1}{R_{DA}}\right) \quad (10)$$

where e, ε_0, ε_{opt}, ε_r, $r_{D(A)}$, and R_{DA} are the elementary charge, the vacuum permittivity, the optical and relative dielectric

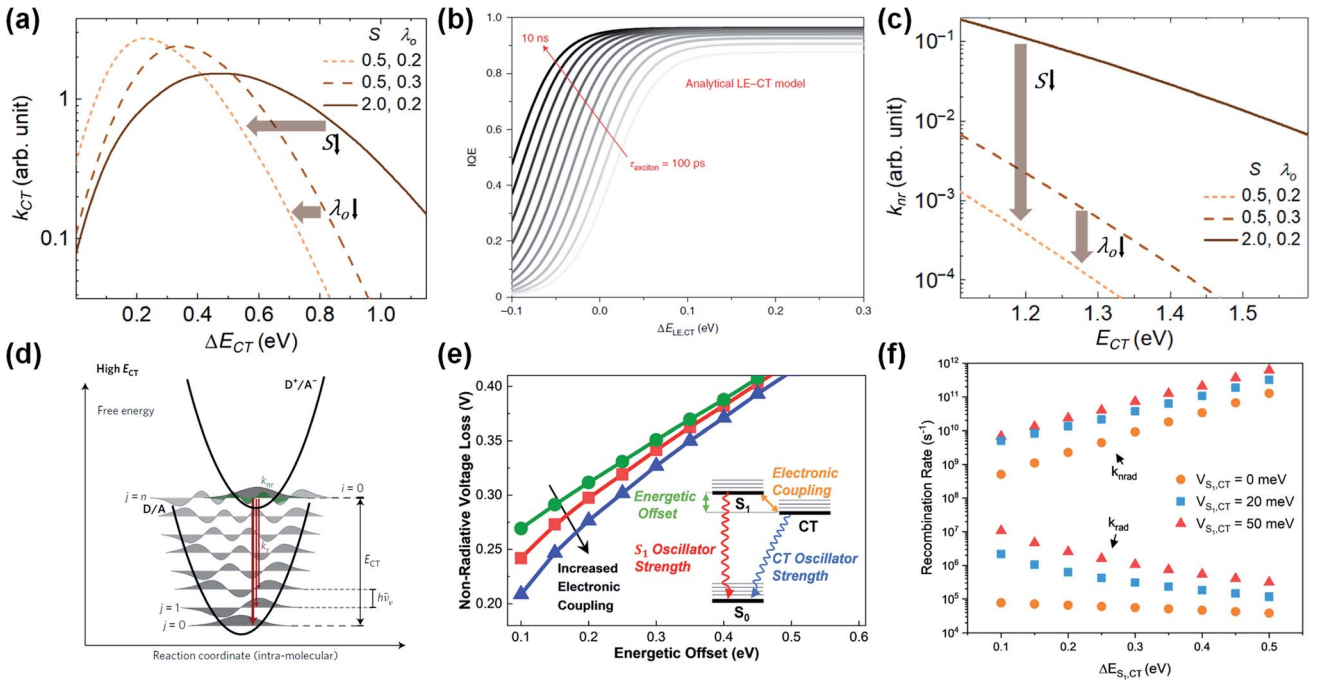

Fig. 5 (a) CT rate (k_{CT}) *versus* energy offset (ΔE_{CT}). The peak k_{CT} occurs as intermolecular reorganization energy (λ_O) and intramolecular coupling strength (S) decrease. S is correlated with intramolecular reorganization energy (λ_I) and is expressed as $S = \lambda_I/\hbar\langle\omega_I\rangle$. Reproduced with permission.[129] Copyright 2019, Elsevier. (b) Calculation of IQE (consistent with exciton-splitting efficiency) based on the energy difference between the lowest excited state (LE is consistent with S_1) and CT state ($\Delta E_{LE,CT}$), and exciton lifetime (τ_{exc}). Reproduced with permission.[139] Copyright 2020, Springer Nature. (c) Non-radiative CT recombination rate (k_{nr}) *versus* E_{CT} as a function of λ_O and S. The k_{nr} decreases as λ_O and S decreases and E_{CT} increases. Reproduced with permission.[129] Copyright 2019, Elsevier Inc. (d) The potential energy of the ground state (D/A) and the CT state (D^+/A^-). Reproduced with permission.[132] Copyright 2017, Springer Nature. (e) Simulated non-radiative recombination voltage loss ($\Delta V_{OC}^{non\text{-}rad}$) *versus* ΔE_{CT} as a function of electronic coupling (hybridization). Inset schematic diagram represents three-state model. (f) Recombination rate *versus* ΔE_{CT} as a function of hybridization. Reproduced with permission.[141] Copyright 2019, American Chemical Society.

constants, the donor (or acceptor) radius, and the distance between the center to center of the donor and the acceptor, respectively. Here, the ε_{opt} is extracted in terms of $\varepsilon_{opt} = n^2$ (n = refractive index),[137] while the ε_r is obtained according to the Clausius–Mossotti equation that comprises molecular polarizability (α) and molecular volume (V):[138]

$$\frac{\varepsilon_r - 1}{\varepsilon_r + 2} = \frac{4\pi}{3}\frac{\alpha}{V} \quad (11)$$

In short, a larger ε_{opt} and ε_r and a smaller R_{DA} can lead to a lower λ_O in the CT state. Furthermore, a large ε_r and an average electron–hole distance (r) will reduce the E_b, resulting in a small ΔE_{CT}. The E_b can be expressed as follows:[138]

$$E_b \approx \frac{e^2}{4\pi\varepsilon_0\varepsilon_r r} \quad (12)$$

The difference in the n of acceptor materials was reported by Kerremans *et al.*, with the ellipsometry measurement revealing higher n values (*i.e.*, ε_{opt}) in NFAs than in conventional FAs (*e.g.*, $n = 2.7$ for IT-4F and $n = 2.2$ for $PC_{71}BM$).[115] Meanwhile, in terms of the ε_r of acceptors, Zhu *et al.* performed a computational study using density functional theory (DFT) and found that planar and rigid A–D–A structures have a higher α (*e.g.*, $\alpha = 247.5$ Å^3, $\varepsilon_r = 5.11$ for IT-4F, and $\alpha = 114.5$ Å^3 and $\varepsilon_r = 3.83$ for $PC_{71}BM$) and a smaller E_b (*e.g.*, $E_b = 0.35$ and 0.90, 0.63 for IT-4F, $PC_{71}BM$, SF-PDI2, respectively) than bulky or spherical structures.[138] In addition, grazing-incidence wide-angle X-ray scattering measurement has been used to reveal that the R_{DA} between the polymer donor and the NFA is close enough for effective intermolecular reorganization (*e.g.*, $R_{DA} = 3.61$ Å for PM6:Y6).[101]

The long exciton lifetime (τ) also plays a critical role in improving the exciton-splitting efficiency in low ΔE_{CT} systems (Fig. 5b). Here, Classen *et al.* examined the lifetime and efficiency of exciton splitting using polymer donor:NFA blends with a ΔE_{HOMO} of 0–0.3 eV, with the NFA-based OPVs exhibiting slow exciton-splitting lifetimes ($\tau_{splitting} > 20$ ps) and high exciton-splitting efficiencies ($\eta_{splitting} > 90\%$) owing to the long τ of NFAs (305.3, 561.5, 898.3, and 1016 ps for ITIC, *o*-IDTBR, EH-IDTBR, and Y6, respectively).[139] This demonstrates that NFAs with a long τ allow for efficient exciton splitting even with a negligible driving force (*i.e.*, $\Delta E_{CT} < 0.2$ eV). In practice, NFA-based OPVs have recently been reported to exhibit high PCEs even with a negligible ΔE_{CT} or ΔE_{HOMO}. For example, the PM6:Y11-based OPV exhibits a PCE of 16.54% despite the ΔE_{CT} of 0 eV,[82] while the PTQ11:TPT10-based OPV exhibits a PCE of 16.32% even at a ΔE_{HOMO} of 0 eV.[140]

4.2.3. CT state recombination. The small wave-function overlap between the $HOMO_D$ and the $LUMO_A$ significantly reduces the oscillator strength of CT excitons, resulting in a comparatively slower k_r than k_{nr}.[132] In other words, CT excitons are decayed primarily through non-radiative recombination (*i.e.*, low EQE_{EL}). The difference in CT oscillator strength between FA- and NFA-based OPVs becomes evident in terms of and EQE_{EL}. Indeed, NFA-based OPVs exhibit a lower $\Delta V_{OC}^{non\text{-}rad}$ (<0.35 V) and a higher EQE_{EL} ($\approx 10^{-4}$) than FA-based OPVs ($\Delta V_{OC}^{non\text{-}rad} = 0.35$–0.46 V, $EQE_{EL} \approx 10^{-6}$–10^{-8}), indicating that NFAs considerably suppress the non-radiative recombination in blend devices.[141]

In addition to lowering the λ_I and λ_O (Fig. 5c),[129,134] increasing the E_{CT} level (*i.e.*, decreasing the ΔE_{CT}) can reduce the k_{nr} (*i.e.*, a smaller $\Delta V_{OC}^{non\text{-}rad}$) because of the smaller wave-function overlap between the CT and the ground state (S_0) (Fig. 5d).[132] Here, Benduhn *et al.* reported a linear regression with a slope of ≈ -0.2 V eV^{-1} between $\Delta V_{OC}^{non\text{-}rad}$ and E_{CT},[132] while Classen *et al.* reported a sharp decrease in $\Delta V_{OC}^{non\text{-}rad}$ with a slope of ≈ -0.6 V eV^{-1} at a ΔE_{HOMO} of less than 0.2 eV.[139] Eisner *et al.* proposed a three-state model in which a small ΔE_{CT} enables electronic coupling (hybridization) between the S_1 and the CT state to enhance the oscillator strength from CT to S_0.[141] As shown in Fig. 5e, the $\Delta V_{OC}^{non\text{-}rad}$ decreases with an increase in hybridization at a given ΔE_{CT}. Consequently, the k_{nr} slows down as the ΔE_{CT} decreases in the absence of hybridization, while the k_r remains almost constant (Fig. 5f). However, the hybridization affects the k_r much more than the k_{nr}, thus increasing the oscillator strength of the CT exciton in low-ΔE_{CT} systems (*i.e.*, higher EQE_{EL}). For example, the PM6:Y11 device has a ΔE_{CT} of 0 eV and exhibits a higher EQE_{EL} ($EQE_{EL} \approx 1.4 \times 10^{-3}$, $\Delta V_{OC}^{non\text{-}rad} = 0.17$ V) than conventional high-performance FA-based OPVs. Moreover, the overall V_{loss} of the PM6:Y11 device is 0.43–0.51 V, which is very close to that of c-Si solar cells (0.38 V).[82]

4.3. Charge transport

4.3.1. Charge transport physics. The charge transport of free charge carriers (*i.e.*, holes and electrons) separated from the excitons is an important factor in determining the charge collection efficiency and is highly related to the J_{SC} and FF parameters. In addition, efficient and balanced charge transport in the blend film, along with suppressed non-geminated recombination, is desirable in terms of improving the charge collection efficiency.[142] However, most organic semiconductors contain a large amount of disordered regions (*i.e.*, amorphous domains),[85,93,143] generating energetic disorders that limit the efficient charge transport. On the other hand, the structural features of NFAs enable efficient electron transport through an increased electron transfer integral ($|J_e|$)[98] or a reduced energetic disorder, and they showed well-balanced charge transport with polymer donor materials.[110]

4.3.2. A–D–A-type non-fullerene acceptors. The planar and rigid structure of A–D–A-type NFAs can provide close intermolecular packing (3–4 Å) and can enhance the structural resilience with low energetic disorders. While the close packing between adjacent molecules is essential for efficient charge transport, effective electronic coupling should be considered because of the different wave-function shapes along the molecular backbone. In other words, an optimal wave-function overlap (*i.e.*, HOMO and HOMO-1 for hole transport, LUMO and LUMO+1 for electron transport) enables effective electronic coupling,[103] thus increasing the $|J|$ of NFAs. In practice, a large displacement between the LUMO and the LUMO+1 in NFAs can result in a lower $|J_e|$ than in FAs (*e.g.*, 11.4 meV for ITIC[98] and 50 meV for $PC_{61}BM$[144]).

Aldrich *et al.* studied the change in μ_e with a number of F substituents at the end-groups of A–D–A-type NFAs (ITIC, ITIC-4F, and ITIC-6F).[98] Here, the DFT calculation revealed that all NFAs have similar electron delocalization but that the LUMO and LUMO+1 are predominantly localized on the end-groups. In the single-crystal analysis, the ITIC and ITIC-6F were found to exhibit face-to-face π–π stacking between the end-groups (≈3.4 Å for ITIC and 3.95, 3.28 Å for ITIC-6F), while the ITIC-4F had a coexisting packing of face-to-face and edge-to-face stacking (3.35 Å) (Fig. 6a). Meanwhile, in addition to the π–π stacking, lone-pair⋯π interactions were observed in the ITIC-4F (S⋯π) and ITIC-6F (CN⋯π), contributing to closer intermolecular packing distances (3.21 Å for ITIC-4F and 3.16 Å for ITIC-6F). Finally, the $|J_e|$ calculated from the crystal dimers was 11.4, 17.1 and 56.8 meV for the ITIC, ITIC-4F and ITIC-6F, respectively, with the ITIC-6F consequently exhibiting a higher μ_e (5.7×10^{-4} cm^2 V^{-1} s^{-1}) than the other two NFAs (3.1×10^{-4} and 5.1×10^{-4} cm^2 V^{-1} s^{-1} for ITIC and ITIC-4F, respectively).

4.3.3. A–D–A′–D–A-type non-fullerene acceptors. The A–D–A′–D–A-type NFA with a curvature structure (*e.g.*, Y6 analogs) has more intermolecular packing modes than A–D–A-type NFAs.[103,104] As noted above, the A–D–A-type NFAs mainly adopt end-group stacking due to the bulky side chains on the core unit. In contrast, Y6 analogs can form multiple packings between the end-groups as well as core units due to the curvature structure and the less bulky alkyl chains (*e.g.*, linear alkyl chain) on the core unit (Fig. 6b).

Zhang *et al.* identified the multiple packings in a Y6 single crystal and obtained the $|J_e|$ from the Y6 dimer packings.[103] Here, the Y6 had a longer intermolecular distance (≈3.5 Å) than had the ITIC-based NFAs but exhibited a larger $|J_e|$ (81 meV) and μ_e (1.8×10^{-4} cm^2 V^{-1} s^{-1}) because of its multiple packing structure. In addition, the core unit packing was found to enhance the overlap between the HOMO and HOMO-1, exhibiting high hole transfer integral ($|J_h|$) (74 meV) and hole mobility (μ_h) (5.6×10^{-4} cm^2 V^{-1} s^{-1}). These features enable the ambipolar charge transport of Y6, which is beneficial for a balanced charge transport in polymer donor:NFA blends. Elsewhere, Hamada *et al.* examined the μ_e and μ_h of PBDB-T based blends,[145] where the PBDB-T:NFA blends exhibited a more balanced charge transport than the PBDB-T:$PC_{71}BM$ blend (μ_h/μ_e = 0.057, 0.95, 1.14 for PBDB-T:$PC_{71}BM$, PBDB-T:Y6 and PBDB-T:ITIC, respectively).

4.3.4. Energetic disorder. The charge transport of organic semiconductors is strongly governed by the hopping mechanism,[146] meaning a large degree of energetic disorder increases the trap density in the amorphous regions, thus boosting the non-geminate recombination. The total energetic disorder (σ) includes dynamic (σ_D) and static energetic disorder (σ_S) and is expressed as $\sigma = \sigma_D^2 + \sigma_S^2$,[147] while the planar and rigid backbone structure (*e.g.*, IDT-based cores) enhances the structural resilience and constructs interconnected aggregates (or small crystallites) with a short-range order.[148,149] Such a morphology provides efficient charge transport with a narrow trap

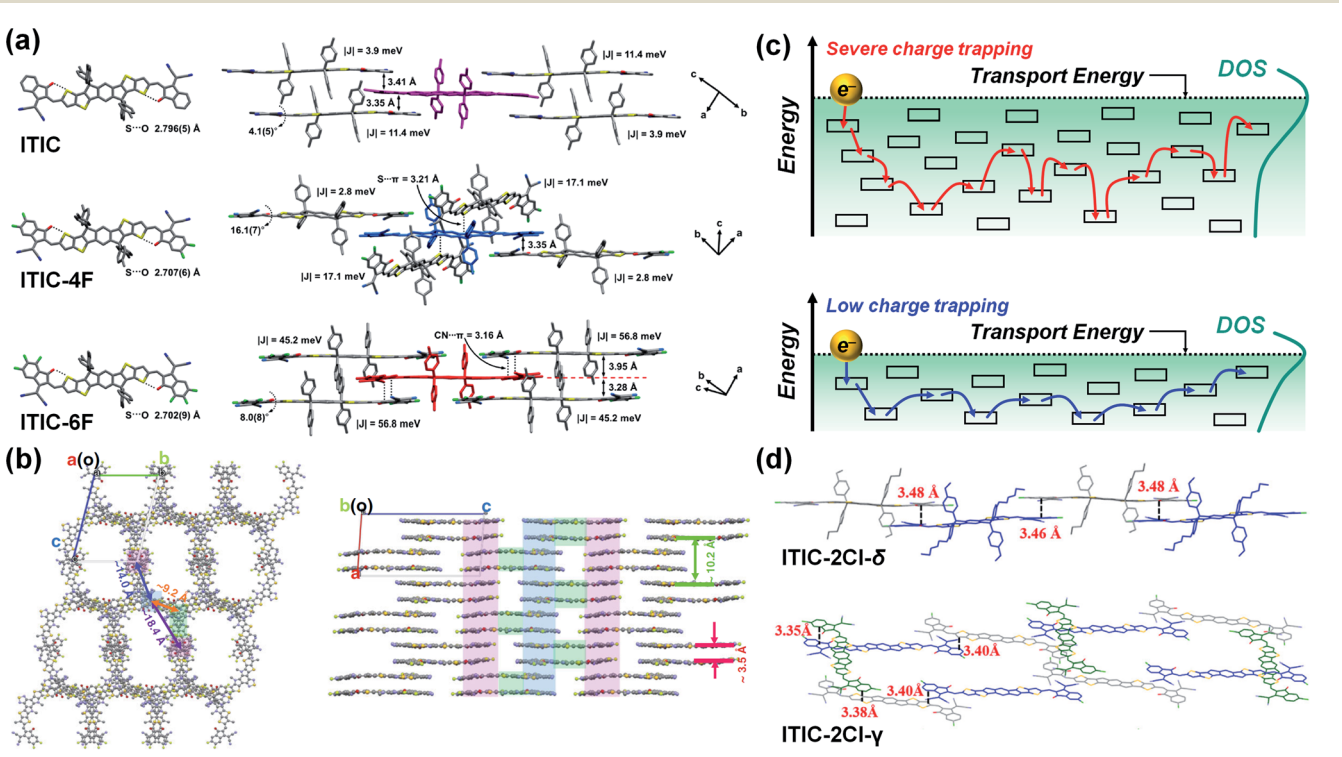

Fig. 6 (a) Single crystal and intermolecular packing structure of ITIC, ITIC-4F, and ITIC-6F. Reproduced with permission.[98] Copyright 2019, American Chemical Society. (b) Crystal packing structure of Y6. Reproduced with permission.[103] Copyright 2020, Springer Nature. (c) Schematic illustration of electron transport for organic semiconductors governed by hopping mechanism (top: large DOS, bottom: small DOS). (d) Molecular packing structure of ITIC-2Cl-δ (top) and ITIC-2Cl-γ (bottom). Reproduced with permission.[152] Copyright 2019, Elsevier.

distribution *via* continuous electrical connections between the aggregates (Fig. 6c).

Kupgan *et al.* quantified the MD and DFT approaches and found that the NFA had a lower σ than the FA through a combination of molecular dynamics (σ = 54, 52, 77 meV for FNIC1, FNIC2, $PC_{71}BM$, respectively).[147,150] The low σ values of NFAs are largely due to the significant decrease in σ_S (24, 25, and 46 meV for FNIC1, FNIC2, and $PC_{71}BM$, respectively), indicating that coplanar and rigid backbone structures are more effective in reducing σ_S than are spherical structures.

Modulating the intermolecular interaction of the NFA can further facilitate cross-stacking, constructing an interconnected network structure that provides 3D charge transport pathways in OPV blends.[93,151] Lai *et al.* introduced Cl atoms to the delta (ITIC-2Cl-δ) or gamma (ITIC-2Cl-γ) position of ITIC end-groups.[152] Here, the ITIC-2Cl-γ crystal exhibited an interconnected network structure containing both linear- and cross-stackings, while the ITIC-2Cl-δ crystal mainly adopted a linear stacked structure (Fig. 6d). Meanwhile, when blended with PBDB-TF, the PBDB-TF:ITIC-2Cl-γ exhibited a higher μ_e (2.6×10^{-4} cm^2 V^{-1} s^{-1}) than did the PBDB-TF:ITIC-2Cl-δ ($\mu_e = 1.2 \times 10^{-4}$ cm^2 V^{-1} s^{-1}). Elsewhere, Zhang *et al.* investigated the energetic disorder of representative polymer-based blends by measuring the Urbach energy (E_U), which represents the trap distribution.[110] Here, the polymer donor:FA blends exhibited a higher E_U (*e.g.*, E_U = 36.0 meV for PffBT4T-2OD:$PC_{71}BM$) than did the polymer donor:NFA blends (*e.g.*, E_U = 34.4 and 22.4 meV for PBDB-T:ITIC and PM6:Y18, respectively). This result demonstrated that the interconnected structure of Y18 efficiently reduces the trap density of OPV blends.

4.4. Triplet-exciton harvesting

4.4.1. Role of triplet excitons. The lowest triplet state (T_1) is typically located approximately 0.6–1 eV below the S_1 and can present a loss source of photo-excited excitons.[153,154] However, triplet excitons have a long L_D of hundreds of nanometers because of their long τ_{exc}, providing sufficient time for CT excitons to separate into free charge carriers.[49,154–157] As such, triplet materials have the latent capability to further improve device performances. To exploit triplet excitons efficiently, the

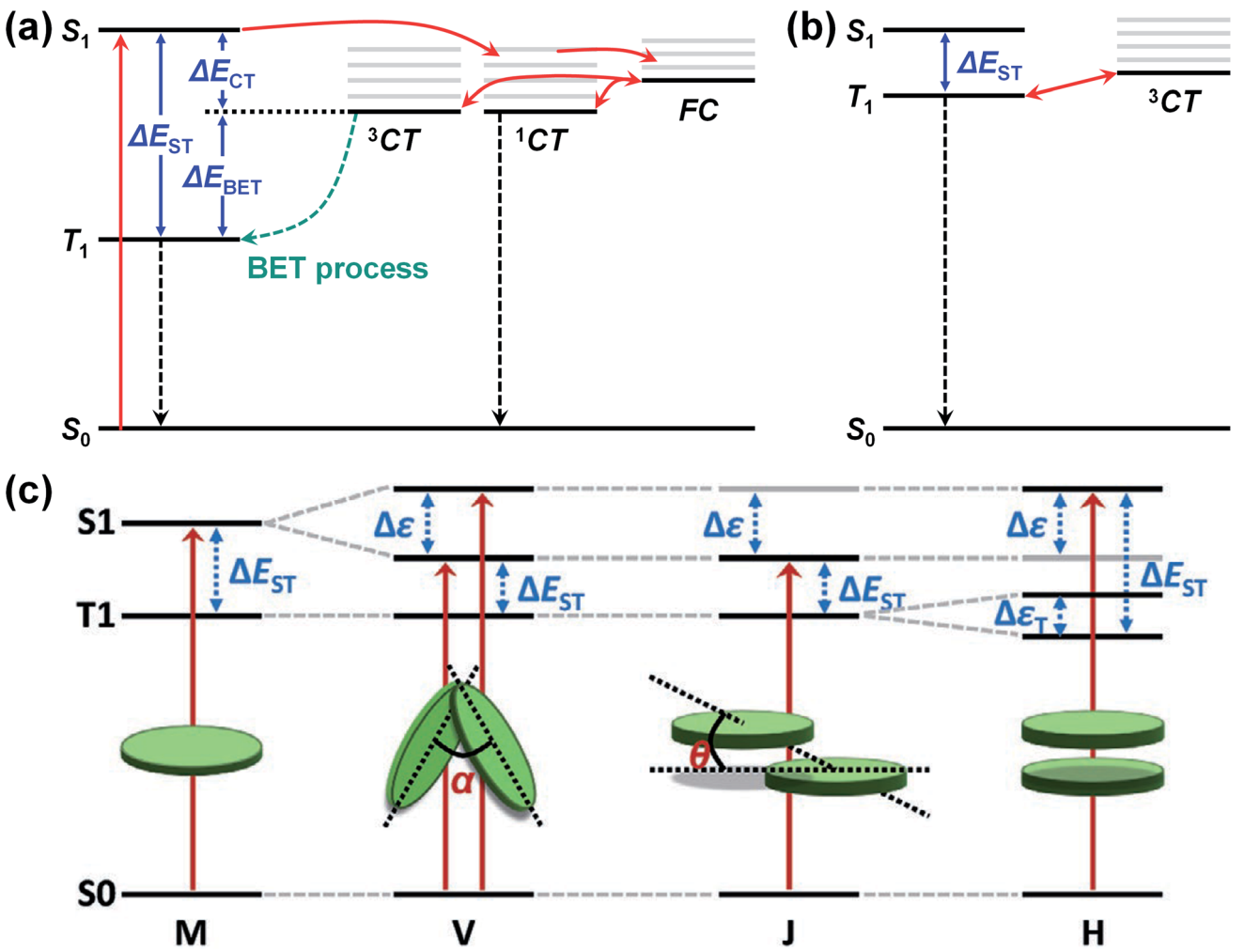

Fig. 7 (a) Schematic illustration of triplet-recombination through back electron transfer (BET) process. (b) Energy diagram with small ΔE_{CT}, ΔE_{ST}, and ΔE_{BET}. (c) Schematic energy diagram of S_1 and T_1 splitting according to molecular packing modes (V-type, J-type, and H-type molecular packing structures). Reproduced with permission.[153] Copyright 2020, WILEY-VCH.

energy difference between the S_1 and T_1 (*i.e.*, $\Delta E_{ST} = E_{S_1} - E_{T_1}$) and the ΔE_{CT} should be as small as possible to prevent an energetically favored back electron transfer (BET) from ^{3}CT to T_1 of the donor or acceptor (Fig. 7a). The BET process causes triplet recombination through triplet–triplet annihilation and is accelerated as the energy difference between the E_{CT} and the E_{T_1} (*i.e.*, $\Delta E_{BET} = |E_{CT} - E_{T_1}|$) increases.[153,158–160] Energy level engineering that increases the T_1 or moves it closer to ^{3}CT has demonstrated the feasibility of suppressing the BET process (Fig. 7b).[157,161]

4.4.2. NFAs with the heavy atom effect. The introduction of heavy atoms (*e.g.*, iridium [Ir] or platinum [Pt]) into π-conjugated molecules enhances the spin–orbit coupling between the S_1 and the T_1, generating triplet excitons through the intersystem crossing (ISC).[162] Such triplet excitons are easily converted to ^{3}CT excitons when the T_1 is higher than the ^{3}CT. To date, polymer donors containing Ir or Pt metals (*e.g.*, poly-DPP-Ph-Pt and poly-DPP-Th-Pt) have been the focus of most reports but have exhibited low device performances because of the poor blend morphology with the acceptor materials (*i.e.*, large-scale phase separation).[155,163]

Meanwhile, Yang *et al.* reported a PDI-based triplet acceptor in which tellurophene was fused with two PDI units (BFPTP).[164] The triplet excitons of the BFPTP were confirmed *via* the photoluminescence (PL) emission with a long lifetime of 24.41 ms at 77 K. The energy level of the T_1 (E_{T_1}) of the BFPTP was 1.50 eV, which is higher than the E_{CT} of PBDB-T:BFPTP (1.45 eV), indicating that triplet excitons can be converted into ^{3}CT excitons. The PBDB-T/BFPTP bilayer device demonstrated that the BFPTP had a long L_D of 34 nm (similar to the L_D of triplet FAs), and, as a result, the PBDB-T:BFPTP-based OPV exhibited a PCE of 7.52%, which was a meaningful result that demonstrated, for the first time, the feasibility of utilizing a triplet NFA.

4.4.3. NFAs with a small ΔE_{ST}. A small ΔE_{ST} (*i.e.*, large spin–orbit coupling) is beneficial to harvesting triplet excitons without heavy atoms, which can be observed in highly twisted structures between the electron-rich and electron-deficient units.[165–167] However, the highly twisted structure of NFAs has drawbacks in terms of inefficient light harvesting and charge transport.[168]

Among the NFA molecules, Y6-derivatives have a slightly twisted structure owing to the sp^2-hybridization of the N atoms in the main backbone and are good candidates for triplet acceptors.[168] Qin *et al.* reported two triplet acceptors, both analogs of Y6 (H1 and H2),[168] and observed long PL decays on the μs scale in both acceptors (8.15 μs for H1 and 7.66 μs for H2 at 77 K). The two NFAs exhibited a relatively small ΔE_{ST} (≈0.35 eV) and had an E_{T_1} (≈1.07 eV) close to the E_{CT} (≈1.37 eV) of blend films employing PBDB-T as a polymer donor. Meanwhile, the transient absorption decay was 65 ns for the PBDB-T:H1 and 35 ns for the PBDB-T:H2, which was much longer than the S_1 decay of each component. The existence of triplet excitons in the PBDB-T:H1 and PBDB-T:H2 devices was confirmed *via* magneto-photocurrent measurement, with both devices exhibiting a high PCE of over 14%.

In addition, the ΔE_{ST} can be controlled *via* the molecular packing mode. In V-type or J-type packing modes (*i.e.*, small intermolecular overlap), the T_1 splitting is negligible, while the S_1 splitting is significant because of the small intermolecular overlap. As shown in Fig. 7c, this splitting difference can reduce the ΔE_{ST}. In contrast, an H-type packing mode (*i.e.*, large intermolecular overlap) can increase the ΔE_{ST} since both the S_1 and the T_1 will be significantly split.[169,170] Elsewhere, Han *et al.* conducted a theoretical study using time-dependent DFT (TD-DFT) calculations in combination with MD simulations and found that the ΔE_{ST} could be reduced by end-group π–π stacking in A–D–A- or A–D–A′–D–A-type NFAs.[153] The calculated ΔE_{ST} of the J-type dimer for IT-4F and Y6 were 0.35 and 0.32 eV, respectively, with the two V-type dimers possessing a similar ΔE_{ST} to the J-type dimers. Compared with the ΔE_{ST} of the monomers (0.44 eV for IT-4F, 0.42 eV for Y6), the J-type and V-type dimers exhibited a decrease in ΔE_{ST} of around 0.1 eV because of the end-group π–π stacking. Meanwhile, because of the reduced ΔE_{ST}, the ΔE_{BET} for PM6:IT-4F and PM6:Y6 was calculated to be 0.13 and 0.23 eV, respectively, indicating that T_1 excitons can assist the regeneration of free charge carriers. Finally, the transfer rate from T_1 to ^{3}CT ($k_{T_1 \rightarrow CT}$) for both blends was estimated to be 10^7–10^9 s^{-1}, while the rate of triplet recombination ($k_{T_1 \rightarrow S_0}$) was calculated to be 4–7 × 10^3 s^{-1}, around 4–6 orders lower than the $k_{T_1 \rightarrow CT}$.

4.5. Blend morphology

4.5.1. Blend miscibility and the Flory–Huggins parameter. The D:A blend films form a three-phase morphology (pure D, pure A, and intermixed phase), with its composition determined by the degree of mixing between the D and the A.[171–173] The blend morphology is highly related to the FF and stability of the OPV device, with the well-mixed blend morphology providing efficient charge transport while suppressing the charge recombination.[174,175] Therefore, understanding the thermodynamics and kinetics of the morphology formation is important for the rational design of blend films.

The phase behavior of the amorphous mixed phase is controlled by the molecular interaction of the D and A. Here, the Flory–Huggins model has been widely used to quantify the degree of mixing between the blend components and has been extended quantitatively to describe the thermodynamic behavior of D:A blends.[173,176,177] The change in the Gibbs free energy of mixing (ΔG_{mix}) in a polymer-containing blend can be expressed by the following equation:[177]

$$\Delta G_{mix} = kT\left(\frac{\emptyset_1}{N_1}\ln \emptyset_1 + \frac{\emptyset_2}{N_2}\ln \emptyset_2 + \chi \emptyset_1 \emptyset_2\right) \quad (13)$$

where $\emptyset$ and N are the volume fraction of the components and the effective molecular sizes of the polymers (*e.g.*, molecular weight or degree of polymerization), respectively, while χ is the Flory–Huggins interaction parameter that quantifies the enthalpic interaction between the mixed components, where the lower the χ value, the higher the degree of molecular mixing. To date, differential scanning calorimetry (DSC),[178] contact angle,[179] solubility parameter,[180,181] and time-of-flight secondary ion mass spectrometry (TOF-SIMS)[179] analyses have been used for determining χ.

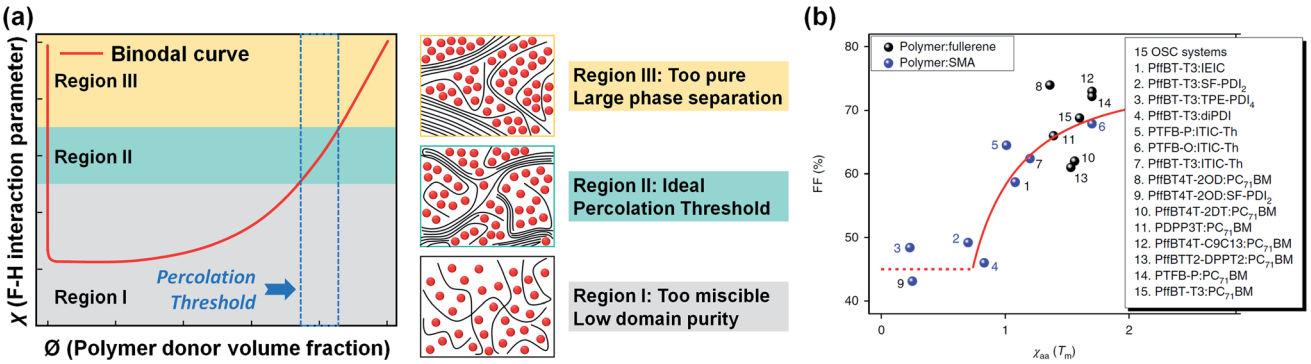

Fig. 8 (a) Schematic illustration of three regions in the binodal curve of the χ–Ø phase diagram; low χ (region I), medium χ (region II), and high χ (region III), respectively. (b) χ parameter estimated from DSC and its relation to FF. Reproduced with permission.[174] Copyright 2018, Springer Nature.

The mixed phase can be divided into three regions in the binodal curve of the χ–Ø phase diagram (Fig. 8a).[174,182] Here, the blend in the low χ region is too miscible and has a low domain purity, while large phase separation occurs when the domains are too pure (*i.e.*, high χ region). These two cases result in performance degradation due to inefficient photocurrent generation paths (*e.g.*, increased charge recombination and low charge collection efficiency). The ideal χ with a binary composition close to the percolation threshold can lead to optimal amorphous miscibility and stable morphology in a thermodynamic equilibrium state; however, most OPV blends exhibit a higher or lower χ that deviates from the ideal χ region.

4.5.2. Blend morphology, device FF and stability. Since the χ plays an important role in morphology formation, the miscibility-device function relationship is of great interest in terms of manipulating a blend composition to determine the optimal χ. Here, Ade *et al.* developed a measurement technique to accurately determine the temperature dependence of the χ (*i.e.*, $\chi[T]$) for representative OPV blends and established a quantitative model of the relationship between the domain purity of the mixed phase and the device FF, which can be expressed by the following equation:[174]

$$\mathrm{FF} \propto \sigma = \sqrt{\mathrm{ISI}} \propto \sqrt{(\emptyset_0 - \emptyset_1)(\emptyset_2 - \emptyset_0)} \qquad (14)$$

where ISI is the integrated scattering intensity of the resonant soft X-ray scattering (R-SoXs), with the square root of the ISI representing the relative domain purity (σ).[192] This model was experimentally verified using 15 types of blend system (*e.g.*, polymer donor:$PC_{71}BM$ and NFA), which indicated a constant-kink-saturation relationship between the χ and the device FF, where the larger the χ, the higher the σ (*i.e.*, stronger phase separation), and, thus, the higher the device FF.[174] In addition, the majority of polymer donor:$PC_{71}BM$ blends exhibit a larger χ and a higher device FF ($1.3 < \chi < 1.7$, 61% < FF < 74%) than do polymer donor:NFA blends ($0.23 < \chi < 1.01$, 46% < FF < 65%) (Fig. 8b and Table 2).

Nevertheless, most of the FA-based OPVs suffer from the so-called "burn-in loss" issue, which causes an initial loss of up to 30–40% of the PCE.[193] These burn-in losses originate from the photoinduced degradation of FAs (*i.e.*, dimerization) and from crystallization, leading to a macroscopic phase separation of the blend film.[194,195] Li *et al.* investigated the de-mixing in polymer donor:$PC_{71}BM$ blends under aging conditions (5 days).[196] Here, using grazing-incidence small-angle X-ray scattering, the $PC_{71}BM$ domain size was found to have increased from 43 nm (the initial blend film) to 78 nm (the aged blend film; 80% increase). As the size of pure the $PC_{71}BM$ domains increased in the aged sample, the volume fraction and size distribution of the $PC_{71}BM$ domains also increased. In other words, the growth of larger clusters and phase separation occurred in the polymer donor:$PC_{71}BM$ blend under the aging condition when the $PC_{71}BM$ molecules diffused out of the amorphous mixed phases.

On the other hand, it has been reported that NFAs suppress the burn-in loss to light and heat owing to their higher chemical stability and miscibility compared with FAs.[86–88,197] Zhu *et al.* characterized the change in the IEICO-4F domain size in the amorphous mixed phase (PTB7-Th:IEICO-4F) under aging conditions (90 days), as measured *via* R-SoXs.[88] The size of the IEICO-4F domains increased from 38 nm (initial blend film) to 43 nm (aged blend film; 13% increase). This indicates that the NFA-based blend system has a more stable film morphology than the FA-based blend system. Furthermore, Du *et al.* reported a promising long-term stability system of NFA blend films with an extrapolated T_{80} lifetime (80% of the initial PCE) of over 11 000 h under one-sun illumination.[197]

4.5.3. Molecular designs for morphology control. Various molecular design strategies for controlling the molecular miscibility have been reported in relation to polymer–NFA domain size, purity, and device FF.[173] In the molecular design of polymer donors, an approach involving an increase in the rigidity of the polymer donor has proven to be effective for the nanoscale-phase separation in blend films without excessive intermixing with NFAs (*i.e.*, higher χ). Here, Li *et al.* investigated the impact of molecular packing on the blend miscibility (polymer donor:IT-4F) by adjusting the alkyl chains of polymer donors (*n*-octyl for P1, *n*-decyl for P2, and 3,7-dimethyloctyl for P3).[189] The P2 polymer with a long linear alkyl chain exhibited lower blend miscibility (χ = 0.25 K, measured in terms of surface energy) than did the other two blends (χ = 0.15 K for P1:IT-4F, χ = 0.19 K for P3:IT-4F) owing to the close

Table 2 OPV performance with χ and ISI value for polymer donor:FA and polymer donor:NFA

Acceptor	Donor	V_{OC} [V]	J_{SC} [mA cm^{-2}]	FF [%]	PCE [%]	χ_{aa}	ISI	Ref.
FAs								
$PC_{71}BM$	PDPP3T	0.66	15.4	66	6.6	1.39 (T_m)[a]	1	174 and 183
$PC_{71}BM$	PTFB-P	0.81	12.9	72	7.5	1.70 (T_m)[a]	—	174 and 184
$PC_{71}BM$	PffBT4T-2DT	0.76	16.2	62	7.6	1.56 (T_m)[a]	—	174 and 185
$PC_{71}BM$	PffBTT2-DPPT2	0.81	17.1	61	8.6	1.53 (T_m)[a]	—	174 and 186
$PC_{71}BM$	PffBT4T-2OD	0.77	18.4	74	10.5	1.36 (T_m)[a]	1	22 and 174
$PC_{71}BM$	PffBT-T3	0.82	18.9	69	10.7	1.60 (T_m)[a]	—	174 and 187
$PC_{71}BM$	PffBT4T-C_9C_{13}	0.78	19.8	73	11.7	1.70 (T_m)[a]	1	23 and 174
PDI-based NFAs								
SF-PDI2	PffBT4T-2OD	0.97	6.9	43	2.9	0.25 (T_m)[a]	—	174
diPDI	PffBT-T3	0.86	12.8	46	5.1	0.83 (T_m)[a]	0.56	174
TPE-PDI4	PffBT-T3	1.02	11.5	48	5.7	0.23 (T_m)[a]	0.32	174
SF-PDI2	PffBT-T3	1.03	12.3	49	6.2	0.70 (T_m)[a]	0.52	174
IDT-based NFAs								
IEIC	PffBT-T3	1.04	12.6	59	7.7	1.08 (T_m)[a]	0.83	174
ITIC-Th	PTFB-P	0.92	15.5	65	9.2	1.01 (T_m)[a]	0.91	174
ITIC-Th	PTFB-O	0.92	17.1	68	10.9	1.70 (T_m)[a]	1	174
IT-DM	PBDB-T	0.96	16.3	69	11.3	2.0 (HSP)[b]	0.83	188
IT-M	PBDB-T	0.94	17.3	71	12.1	2.7 (HSP)[b]	0.97	188
IT-4F	P1	0.90	20.1	64	11.5	0.15 K[c]	—	189
IT-4F	P2	0.90	20.7	76	14.2	0.25 K[c]	—	189
IT-4F	P3	0.90	20.3	61	11.2	0.19 K[c]	—	189
Y6-based NFAs								
Y6	PM6	0.86	25.5	72	15.8	0.20 K[c]	—	190
Y6	PM1	0.87	25.9	78	17.6	0.26 K[c]	—	190
BTP-4Cl	P3HT	0.50	5.16	39	1.01	2.52 (HSP)[b]	—	191
ZY-4Cl	P3HT	0.88	16.5	65	9.46	2.56 (HSP)[b]	—	191

[a] The value obtained from DSC. [b] HSP. [c] Contact angle measurement.

intermolecular packing. The P2:IT-4F device also exhibited an FF of 70% and maintained 80% of the initial PCE for 2000 min under one-sun illumination. Elsewhere, Wu *et al.* synthesized a PM6-based random copolymer (PM1) containing 20 mol% thiophene–thiazolothiazole, a highly planar moiety.[190] Here, the incorporation of the planar moiety increased the polymer rigidity and reduced the blend miscibility (χ = 0.26 K for PM1:Y6, χ = 0.20 K for PM6:Y6). Meanwhile, a more obvious phase separation with an interpenetrating network morphology was observed in the PM1:Y6 blend than in the PM6:Y6 blend, with a higher FF obtained from the PM1:Y6 device (FF = 78% and 72% for PM1:Y6 and PM6:Y6, respectively).

In terms of NFA design, Li *et al.* extended the π-conjugation of an IDTI by replacing the phenyls with naphthyls (IDTN) to enhance the intermolecular packing.[198] Here, the PBDB-TF:IDTN blend film had a much longer π–π coherence length (9.4 nm) in the out-of-plane direction than the reported PBDB-T-based blend film (1–5 nm),[188,199] while a larger domain size was observed in the PBDB-TF:IDTN blend (65.5 nm) than in the PBDB-TF:IDTI blend, which was due to the more ordered molecular packing of IDTN. The PBDB-TF:IDTN device also exhibited an improved FF (78%) compared with the PBDB-TF:IDTI device (57%).

Chemical substitutions at the end-group of NFAs have also been reported to be effective in increasing the intermolecular interactions. Here, Yang *et al.* substituted the cyano groups in BTP-4Cl-12 with oxygen atoms (ZY-4Cl) and confirmed that ZY-4Cl lowered the miscibility with P3HT through the weak endo/exothermic peak in the DSC curve (no peak in P3HT:BTP-4Cl-12).[191] The χ values obtained from the Hansen solubility parameters (HSPs) were 2.52 and 2.56 for P3HT:BTP-4Cl-12 and P3HT:ZY-4Cl, respectively, indicating the enhanced phase separation in P3HT:ZY-4Cl. Meanwhile, the P3HT:ZY-4Cl blend morphology contributed a higher efficient exciton probability (81% for P3HT:ZY-4Cl, 34% for P3HT:BTP-4Cl-12) and an improved device FF of 65% (FF = 39% in the P3HT:BTP-4Cl-12 device).

5. Summary and outlook

Largely because of the advances in NFA material design, NFA-based OPVs have demonstrated significant improvements in device performance. Specifically, NFA-based OPVs have achieved remarkable increases in the J_{SC} and V_{OC} parameters, which far exceed those of FA-based OPVs. This comprehensive review of the studies on NFAs conducted over the past decade revealed the optimal photophysical, electrical, and morphological characteristics for high-performance OPVs. The distinctive physical features and the current understandings in the field can be summarized as follows:

(1) Light harvesting is the key factor in determining the J_{SC}. Overall, NFAs have smaller E_g and larger α values compared with FAs, which enhances the photon absorption. Meanwhile, NFA-based OPVs with an E_g of 1.2–1.6 eV achieve a high J_{SC} of >20 mA cm^{-2} by covering a wide region (400–1100 nm) through complementary light absorption with the polymer donors. In addition, the long L_D of the NFA offers the feasibility of photocurrent generation even in thick photoactive layers (*i.e.*, almost equal to a micrometer scale).

(2) The CT state of a blend system promotes exciton dissociation, but a large ΔE_{CT} generates substantial V_{loss}. Here, NFAs with a low λ_I and λ_O provide effective charge-separation, even in blend systems with a small ΔE_{CT} (<0.2 eV). In addition, the small ΔE_{CT} of NFA-based blends entails a decrease in $\Delta V^{non\text{-}rad}{}_{OC}$ through the hybridization between the S_1 and CT states in the blends, efficiently lowering the V_{loss} (<0.8 V) compared with that in FA-based blends (0.6–1.2 V).

(3) Overall, NFAs effectively improve the $|J|$ through end-group π–π stacking (*i.e.*, A–D–A-type NFAs) or multiple stacking (*i.e.*, A–D–A′–D–A-type NFAs). Moreover, the planar and rigid conformation of NFAs enhances the structural resilience and facilitates close intermolecular packing, enabling efficient charge transport with a low degree of energetic disorder (*i.e.*, narrow trap distribution).

(4) The NFAs with heavy atoms or a small ΔE_{ST} can become strong candidates for photocurrent generation by harvesting triplet excitons with a long L_D; however, they can also present a loss source for photo-excited excitons when the T_1 of the donor or acceptor is lower than the ^{3}CT (*i.e.*, the BET process). Engineering the electronic structure of NFAs to increase the T_1 or move it closer to the ^{3}CT effectively exploits the triplet excitons.

(5) The majority of NFAs are more miscible with polymer donors than are FAs (*i.e.*, lower χ), while blends tend to have low domain purity. Molecular designs aimed at enhancing the intermolecular packing of the polymer donors or NFAs can increase the domain purity of the blend, thus improving the device FF. In terms of device degradation, NFA-based OPVs exhibit superior operation under photo and thermal stress due to the high chemical stability of the NFAs.

Advances in material design and device fabrications have led to significant improvements in OPV performance, often exceeding 18%, which is comparable to the panel efficiency of polycrystalline silicon PV cells, *i.e.*, 18–20% efficiency for a standard size 60-cell panel (1 × 1.65 m). Along with the design of NFAs, multi-faceted studies covering the development of other layer materials (*e.g.*, donor materials, electron/hole transport materials) and device fabrication (*e.g.*, optimization of device structure, film processing techniques) are still essential to maximize OPV performance. However, many challenges remain in the commercialization of OPV technology with regard to the mass production of photoactive materials and the manufacture of large-scale PV cells with long-term stability.

In terms of the materials for mass production, the current commercially available photoactive materials involve high costs ($2000–3000 g^{-1}), largely owing to the multi-step synthesis that consists of more than 10 steps.[200–202] In fact, the synthesis of most photoactive materials involves palladium-catalyzed cross-coupling reactions (*e.g.*, Suzuki or Stille coupling) and low-temperature reactions at −78 °C, which is undesirable both in terms of productivity and the environment. Therefore, a short-step synthesis using precious-metal-free catalysts and moderate reaction conditions is required for the mass production of photoactive materials. Another consideration is processability through the use of green solvents, given that most photoactive materials are highly soluble in toxic, halogenated solvents (*e.g.*, chloroform, chlorobenzene).

The large-scale fabrication of OPVs is also a challenging issue. Numerous high-performance OPVs have been demonstrated in small-area devices, mainly in the order of mm^2, using spin-coating methods. However, spin-coating is a non-scalable deposition method involving high material waste, and is not suitable for large-scale fabrication using a continuous deposition process.[201] Among the current methods, slot-die coating has demonstrated great potential in terms of an upscaling deposition *via* roll-to-roll fabrication; however, the low efficiency, small cell area, brittle substrate (*e.g.*, ITO-coated PET sheets), and thermal evaporation are limiting a further increase in the manufacturing scale. Hence, the development of novel upscaling deposition techniques (high efficiency of >10% and large cell area of >1 cm^2) and fully roll-to-roll process designs (vacuum-free process, ITO-free device architecture) is crucial for the large-scale fabrication of OPVs. Moreover, the long-term stability of the devices is an essential consideration for commercial manufacturing. Given that the performance warranty of conventional silicon solar panels is 80% of the initial performance over 25 years, a performance lifetime of >10 years is recommended for OPVs.

Aside from the material and cell fabrication perspectives, the origin of the photocurrent generation in OPVs has not yet been fully understood, largely because of the physical complexity of the organic-based blend system. Thus, advanced analytical techniques with high temporal and spatial resolutions are required to allow for clearly and accurately characterizing the physical features of OPV operations. In addition, computational studies using machine learning have recently demonstrated powerful techniques for understanding and predicting the physical properties of the relevant materials and blends while reducing both the time and the cost.[203,204] Therefore, a combination of these two techniques is expected to provide a better understanding of the fundamentals in view of designing more efficient and stable OPVs.

Author contributions

All authors contributed to bibliographic research, discussion, writing, and revision of the article.

Conflicts of interest

There are no conflicts to declare.

Acknowledgements

This research was supported by the National Research Foundation of Korea (NRF) grant funded by the Ministry of Science and ICT (MSIT) (Code No. 2021R1A2C3004420, 2021R1A5A1084921, 2020M3H4A1A02084908).

Notes and references

1 K. A. Mazzio and C. K. Luscombe, *Chem. Soc. Rev.*, 2015, **44**, 78–90.
2 K. Wang, C. Liu, T. Meng, C. Yi and X. Gong, *Chem. Soc. Rev.*, 2016, **45**, 2937–2975.
3 K. Fukuda, K. Yu and T. Someya, *Adv. Energy Mater.*, 2020, **10**, 2000765.
4 J. Qin, L. Lan, S. Chen, F. Huang, H. Shi, W. Chen, H. Xia, K. Sun and C. Yang, *Adv. Funct. Mater.*, 2020, **30**, 2002529.
5 Y. Li, G. Xu, C. Cui and Y. Li, *Adv. Energy Mater.*, 2018, **8**, 1701791.
6 S.-Y. Chang, P. Cheng, G. Li and Y. Yang, *Joule*, 2018, **2**, 1039–1054.
7 P. Cheng and Y. Yang, *Acc. Chem. Res.*, 2020, **53**, 1218–1228.
8 G. Zhang, J. Zhao, P. C. Y. Chow, K. Jiang, J. Zhang, Z. Zhu, J. Zhang, F. Huang and H. Yan, *Chem. Rev.*, 2018, **118**, 3447–3507.
9 Y. Wang, J. Lee, X. Hou, C. Labanti, J. Yan, E. Mazzolini, A. Parhar, J. Nelson, J. S. Kim and Z. Li, *Adv. Energy Mater.*, 2021, **11**, 2003002.
10 M. Wright, R. Lin, M. J. Y. Tayebjee and G. Conibeer, *Sol. RRL*, 2017, **1**, 1700035.
11 M. D. M. Faure and B. H. Lessard, *J. Mater. Chem. C*, 2021, **9**, 14–40.
12 W. Cao and J. Xue, *Energy Environ. Sci.*, 2014, **7**, 2123.
13 L. Zhan, S. Li, X. Xia, Y. Li, X. Lu, L. Zuo, M. Shi and H. Chen, *Adv. Mater.*, 2021, **33**, 2007231.
14 Y. Lin, Y. Firdaus, F. H. Isikgor, M. I. Nugraha, E. Yengel, G. T. Harrison, R. Hallani, A. El-Labban, H. Faber, C. Ma, X. Zheng, A. Subbiah, C. T. Howells, O. M. Bakr, I. McCulloch, S. D. Wolf, L. Tsetseris and T. D. Anthopoulos, *ACS Energy Lett.*, 2020, **5**, 2935–2944.
15 Q. Liu, Y. Jiang, K. Jin, J. Qin, J. Xu, W. Li, J. Xiong, J. Liu, Z. Xiao, K. Sun, S. Yang, X. Zhang and L. Ding, *Sci. Bull.*, 2020, **65**, 272–275.
16 Y. Cui, H. Yao, J. Zhang, K. Xian, T. Zhang, L. Hong, Y. Wang, Y. Xu, K. Ma, C. An, C. He, Z. Wei, F. Gao and J. Hou, *Adv. Mater.*, 2020, **32**, 1908205.
17 C. Li, J. Zhou, J. Song, J. Xu, H. Zhang, X. Zhang, J. Guo, L. Zhu, D. Wei, G. Han, J. Min, Y. Zhang, Z. Xie, Y. Yi, H. Yan, F. Gao, F. Liu and Y. Sun, *Nat. Energy*, 2021, **6**, 605–613.
18 G. Yu, J. Gao, J. C. Hummelen, F. Wudl and A. J. Heeger, *Science*, 1995, **270**, 1789–1791.
19 G. Yu and A. J. Heeger, *J. Appl. Phys.*, 1995, **78**, 4510–4515.
20 A. Wadsworth, Z. Hamid, J. Kosco, N. Gasparini and I. McCulloch, *Adv. Mater.*, 2020, **32**, 2001763.
21 Z. He, B. Xiao, F. Liu, H. Wu, Y. Yang, S. Xiao, C. Wang, T. P. Russell and Y. Cao, *Nat. Photonics*, 2015, **9**, 174–179.
22 Y. Liu, J. Zhao, Z. Li, C. Mu, W. Ma, H. Hu, K. Jiang, H. Lin, H. Ade and H. Yan, *Nat. Commun.*, 2014, **5**, 5293.
23 J. Zhao, Y. Li, G. Yang, K. Jiang, H. Lin, H. Ade, W. Ma and H. Yan, *Nat. Energy*, 2016, **1**, 15027.
24 J. Huang, H. Tang, C. Yan and G. Li, *Cell Rep. Phys. Sci.*, 2021, **2**, 100292.
25 R. S. Gurney, D. G. Lidzey and T. Wang, *Rep. Prog. Phys.*, 2019, **82**, 036601.
26 P. Cheng, G. Li, X. Zhan and Y. Yang, *Nat. Photonics*, 2018, **12**, 131–142.
27 J. Hou, O. Inganas, R. H. Friend and F. Gao, *Nat. Mater.*, 2018, **17**, 119–128.
28 Z. Zhang, J. Yuan, Q. Wei and Y. Zou, *Front. Chem.*, 2018, **6**, 414.
29 A. Armin, W. Li, O. J. Sandberg, Z. Xiao, L. Ding, J. Nelson, D. Neher, K. Vandewal, S. Shoaee, T. Wang, H. Ade, T. Heumüller, C. Brabec and P. Meredith, *Adv. Energy Mater.*, 2021, **11**, 20003570.
30 A. Karki, A. J. Gillett, R. H. Friend and T. Q. Nguyen, *Adv. Energy Mater.*, 2020, **11**, 2003441.
31 J. Zhao, C. Yao, M. U. Ali, J. Miao and H. Meng, *Mater. Chem. Front.*, 2020, **4**, 3487–3504.
32 J. Zhang, H. S. Tan, X. Guo, A. Facchetti and H. Yan, *Nat. Energy*, 2018, **3**, 720–731.
33 H. Sun, F. Chen and Z.-K. Chen, *Mater. Today*, 2019, **24**, 94–118.
34 Y. Lin and X. Zhan, *Mater. Horiz.*, 2014, **1**, 470–488.
35 A. Wadsworth, M. Moser, A. Marks, M. S. Little, N. Gasparini, C. J. Brabec, D. Baran and I. McCulloch, *Chem. Soc. Rev.*, 2019, **48**, 1596–1625.
36 S. Li, C.-Z. Li, M. Shi and H. Chen, *ACS Energy Lett.*, 2020, **5**, 1554–1567.
37 R. Yu, H. Yao, Y. Cui, L. Hong, C. He and J. Hou, *Adv. Mater.*, 2019, **31**, 1902302.
38 J. Gao, J. Wang, Q. An, X. Ma, Z. Hu, C. Xu, X. Zhang and F. Zhang, *Sci. China: Chem.*, 2019, **63**, 83–91.
39 J. Song, C. Li, L. Zhu, J. Guo, J. Xu, X. Zhang, K. Weng, K. Zhang, J. Min, X. Hao, Y. Zhang, F. Liu and Y. Sun, *Adv. Mater.*, 2019, **31**, 1905645.
40 Q. An, J. Wang, W. Gao, X. Ma, Z. Hu, J. Gao, C. Xu, M. Hao, X. Zhang, C. Yang and F. Zhang, *Sci. Bull.*, 2020, **65**, 538–545.
41 L. Chang, M. Sheng, L. Duan and A. Uddin, *Org. Electron.*, 2021, **90**, 106063.
42 M. C. Scharber and N. S. Sariciftci, *Prog. Polym. Sci.*, 2013, **38**, 1929–1940.
43 Y. Cui, C. Yang, H. Yao, J. Zhu, Y. Wang, G. Jia, F. Gao and J. Hou, *Adv. Mater.*, 2017, **29**, 1703080.
44 Z. Xiao, X. Jia, D. Li, S. Wang, X. Geng, F. Liu, J. Chen, S. Yang, T. P. Russell and L. Ding, *Sci. Bull.*, 2017, **62**, 1494–1496.
45 Y. Xie, R. Xia, T. Li, L. Ye, X. Zhan, H. L. Yip and Y. Sun, *Small Methods*, 2019, **3**, 1900424.
46 S. Dai and X. Zhan, *Adv. Energy Mater.*, 2018, **8**, 1800002.
47 W. Wang, C. Yan, T. K. Lau, J. Wang, K. Liu, Y. Fan, X. Lu and X. Zhan, *Adv. Mater.*, 2017, **29**, 1701308.

48 T. Li, S. Dai, Z. Ke, L. Yang, J. Wang, C. Yan, W. Ma and X. Zhan, *Adv. Mater.*, 2018, **30**, 1705969.
49 G. Han and Y. Yi, *Adv. Theory Simul.*, 2019, **2**, 1900067.
50 T. Fukuhara, Y. Tamai and H. Ohkita, *Sustainable Energy Fuels*, 2020, **4**, 4321–4351.
51 H. Hoppe and N. S. Sariciftci, *J. Mater. Res.*, 2011, **19**, 1924–1945.
52 O. Almora, D. Baran, G. C. Bazan, C. Berger, C. I. Cabrera, K. R. Catchpole, S. Erten-Ela, F. Guo, J. Hauch, A. W. Y. Ho-Baillie, T. J. Jacobsson, R. A. J. Janssen, T. Kirchartz, N. Kopidakis, Y. Li, M. A. Loi, R. R. Lunt, X. Mathew, M. D. McGehee, J. Min, D. B. Mitzi, M. K. Nazeeruddin, J. Nelson, A. F. Nogueira, U. W. Paetzold, N. G. Park, B. P. Rand, U. Rau, H. J. Snaith, E. Unger, L. Vaillant-Roca, H. L. Yip and C. J. Brabec, *Adv. Energy Mater.*, 2020, **11**, 2002774.
53 C. Yan, S. Barlow, Z. Wang, H. Yan, A. K.-Y. Jen, S. R. Marder and X. Zhan, *Nat. Rev. Mater.*, 2018, **3**, 18003.
54 N. Zink-Lorre, E. Font-Sanchis, A. Sastre-Santos and F. Fernandez-Lazaro, *Chem. Commun.*, 2020, **56**, 3824–3838.
55 V. Sharma, J. D. B. Koenig and G. C. Welch, *J. Mater. Chem. A*, 2021, **9**, 6775–6789.
56 J. Wang and X. Zhan, *Trends Chem.*, 2019, **1**, 869–881.
57 X. Zhan, A. Facchetti, S. Barlow, T. J. Marks, M. A. Ratner, M. R. Wasielewski and S. R. Marder, *Adv. Mater.*, 2011, **23**, 268–284.
58 D. Zou, F. Yang, Q. Zhuang, M. Zhu, Y. Chen, G. You, Z. Lin, H. Zhen and Q. Ling, *ChemSusChem*, 2019, **12**, 1155–1161.
59 K. Jiang, F. Wu, H. Yu, Y. Yao, G. Zhang, L. Zhu and H. Yan, *J. Mater. Chem. A*, 2018, **6**, 16868–16873.
60 D. Wang, T. Ye and Y. Zhang, *J. Mater. Chem. A*, 2020, **8**, 20819–20848.
61 A. Sharenko, C. M. Proctor, T. S. van der Poll, Z. B. Henson, T. Q. Nguyen and G. C. Bazan, *Adv. Mater.*, 2013, **25**, 4403–4406.
62 Y. Lin and X. Zhan, *Adv. Energy Mater.*, 2015, **5**, 1501063.
63 R. Singh, J. Lee, M. Kim, P. E. Keivanidis and K. Cho, *J. Mater. Chem. A*, 2017, **5**, 210–220.
64 Y. Zhong, M. T. Trinh, R. Chen, G. E. Purdum, P. P. Khlyabich, M. Sezen, S. Oh, H. Zhu, B. Fowler, B. Zhang, W. Wang, C. Y. Nam, M. Y. Sfeir, C. T. Black, M. L. Steigerwald, Y. L. Loo, F. Ng, X. Y. Zhu and C. Nuckolls, *Nat. Commun.*, 2015, **6**, 8242.
65 Y. Zang, C. Z. Li, C. C. Chueh, S. T. Williams, W. Jiang, Z. H. Wang, J. S. Yu and A. K.-Y. Jen, *Adv. Mater.*, 2014, **26**, 5708–5714.
66 D. Sun, D. Meng, Y. Cai, B. Fan, Y. Li, W. Jiang, L. Huo, Y. Sun and Z. Wang, *J. Am. Chem. Soc.*, 2015, **137**, 11156–11162.
67 D. Meng, D. Sun, C. Zhong, T. Liu, B. Fan, L. Huo, Y. Li, W. Jiang, H. Choi, T. Kim, J. Y. Kim, Y. Sun, Z. Wang and A. J. Heeger, *J. Am. Chem. Soc.*, 2016, **138**, 375–380.
68 J. Zhao, Y. Li, H. Lin, Y. Liu, K. Jiang, C. Mu, T. Ma, J. Y. Lin Lai, H. Hu, D. Yu and H. Yan, *Energy Environ. Sci.*, 2015, **8**, 520–525.
69 J. Liu, S. Chen, D. Qian, B. Gautam, G. Yang, J. Zhao, J. Bergqvist, F. Zhang, W. Ma, H. Ade, O. Inganäs, K. Gundogdu, F. Gao and H. Yan, *Nat. Energy*, 2016, **1**, 16089.
70 Q. Wu, D. Zhao, A. M. Schneider, W. Chen and L. Yu, *J. Am. Chem. Soc.*, 2016, **138**, 7248–7251.
71 Y. Duan, X. Xu, H. Yan, W. Wu, Z. Li and Q. Peng, *Adv. Mater.*, 2017, **29**, 1605115.
72 J. Zhang, Y. Li, J. Huang, H. Hu, G. Zhang, T. Ma, P. C. Y. Chow, H. Ade, D. Pan and H. Yan, *J. Am. Chem. Soc.*, 2017, **139**, 16092–16095.
73 H. Hu, Y. Li, J. Zhang, Z. Peng, L. k. Ma, J. Xin, J. Huang, T. Ma, K. Jiang, G. Zhang, W. Ma, H. Ade and H. Yan, *Adv. Energy Mater.*, 2018, **8**, 1800234.
74 K. Kawashima, Y. Tamai, H. Ohkita, I. Osaka and K. Takimiya, *Nat. Commun.*, 2015, **6**, 10085.
75 Y. Cui, H. Yao, L. Hong, T. Zhang, Y. Xu, K. Xian, B. Gao, J. Qin, J. Zhang, Z. Wei and J. Hou, *Adv. Mater.*, 2019, **31**, 1808356.
76 H. Yao, Y. Cui, D. Qian, C. S. Ponseca Jr, A. Honarfar, Y. Xu, J. Xin, Z. Chen, L. Hong, B. Gao, R. Yu, Y. Zu, W. Ma, P. Chabera, T. Pullerits, A. Yartsev, F. Gao and J. Hou, *J. Am. Chem. Soc.*, 2019, **141**, 7743–7750.
77 W. Zhao, S. Li, H. Yao, S. Zhang, Y. Zhang, B. Yang and J. Hou, *J. Am. Chem. Soc.*, 2017, **139**, 7148–7151.
78 S.-S. Wan, X. Xu, Z. Jiang, J. Yuan, A. Mahmood, G.-Z. Yuan, K.-K. Liu, W. Ma, Q. Peng and J.-L. Wang, *J. Mater. Chem. A*, 2020, **8**, 4856–4867.
79 Q. Fan, W. Su, M. Zhang, J. Wu, Y. Jiang, X. Guo, F. Liu, T. P. Russell, M. Zhang and Y. Li, *Sol. RRL*, 2019, **3**, 1900169.
80 L. Hong, H. Yao, Z. Wu, Y. Cui, T. Zhang, Y. Xu, R. Yu, Q. Liao, B. Gao, K. Xian, H. Y. Woo, Z. Ge and J. Hou, *Adv. Mater.*, 2019, **31**, 1903441.
81 Y. Cui, H. Yao, L. Hong, T. Zhang, Y. Tang, B. Lin, K. Xian, B. Gao, C. An, P. Bi, W. Ma and J. Hou, *Natl. Sci. Rev.*, 2020, **7**, 1239–1246.
82 S. Liu, J. Yuan, W. Deng, M. Luo, Y. Xie, Q. Liang, Y. Zou, Z. He, H. Wu and Y. Cao, *Nat. Photonics*, 2020, **14**, 300–305.
83 G. Forti, A. Nitti, P. Osw, G. Bianchi, R. Po and D. Pasini, *Int. J. Mol. Sci.*, 2020, **21**, 8085.
84 Y. Lin and X. Zhan, *Acc. Chem. Res.*, 2016, **49**, 175–183.
85 D. Venkateshvaran, M. Nikolka, A. Sadhanala, V. Lemaur, M. Zelazny, M. Kepa, M. Hurhangee, A. J. Kronemeijer, V. Pecunia, I. Nasrallah, I. Romanov, K. Broch, I. McCulloch, D. Emin, Y. Olivier, J. Cornil, D. Beljonne and H. Sirringhaus, *Nature*, 2014, **515**, 384–388.
86 H. Cha, J. Wu, A. Wadsworth, J. Nagitta, S. Limbu, S. Pont, Z. Li, J. Searle, M. F. Wyatt, D. Baran, J. S. Kim, I. McCulloch and J. R. Durrant, *Adv. Mater.*, 2017, **29**, 1701156.
87 N. Gasparini, M. Salvador, S. Strohm, T. Heumueller, I. Levchuk, A. Wadsworth, J. H. Bannock, J. C. de Mello, H.-J. Egelhaaf, D. Baran, I. McCulloch and C. J. Brabec, *Adv. Energy Mater.*, 2017, **7**, 17007700.
88 Y. Zhu, A. Gadisa, Z. Peng, M. Ghasemi, L. Ye, Z. Xu, S. Zhao and H. Ade, *Adv. Energy Mater.*, 2019, **9**, 1900376.
89 J. Wang and X. Zhan, *Acc. Chem. Res.*, 2021, **54**, 132–143.
90 S. Dai, T. Li, W. Wang, Y. Xiao, T. K. Lau, Z. Li, K. Liu, X. Lu and X. Zhan, *Adv. Mater.*, 2018, **30**, 1706571.

91 B. Jia, J. Wang, Y. Wu, M. Zhang, Y. Jiang, Z. Tang, T. P. Russell and X. Zhan, *J. Am. Chem. Soc.*, 2019, **141**, 19023–19031.
92 C. Cui, *Front. Chem.*, 2018, **6**, 404.
93 D. Li, X. Zhang, D. Liu and T. Wang, *J. Mater. Chem. A*, 2020, **8**, 15607–15619.
94 Y. Lin, F. Zhao, Q. He, L. Huo, Y. Wu, T. C. Parker, W. Ma, Y. Sun, C. Wang, D. Zhu, A. J. Heeger, S. R. Marder and X. Zhan, *J. Am. Chem. Soc.*, 2016, **138**, 4955–4961.
95 Y. Lin, Q. He, F. Zhao, L. Huo, J. Mai, X. Lu, C. J. Su, T. Li, J. Wang, J. Zhu, Y. Sun, C. Wang and X. Zhan, *J. Am. Chem. Soc.*, 2016, **138**, 2973–2976.
96 S. Dai, F. Zhao, Q. Zhang, T. K. Lau, T. Li, K. Liu, Q. Ling, C. Wang, X. Lu, W. You and X. Zhan, *J. Am. Chem. Soc.*, 2017, **139**, 1336–1343.
97 H. Zhang, H. Yao, J. Hou, J. Zhu, J. Zhang, W. Li, R. Yu, B. Gao, S. Zhang and J. Hou, *Adv. Mater.*, 2018, **30**, 1800613.
98 T. J. Aldrich, M. Matta, W. Zhu, S. M. Swick, C. L. Stern, G. C. Schatz, A. Facchetti, F. S. Melkonyan and T. J. Marks, *J. Am. Chem. Soc.*, 2019, **141**, 3274–3287.
99 X. Song, N. Gasparini, L. Ye, H. Yao, J. Hou, H. Ade and D. Baran, *ACS Energy Lett.*, 2018, **3**, 669–676.
100 J. Yuan, Y. Zhang, L. Zhou, C. Zhang, T. K. Lau, G. Zhang, X. Lu, H. L. Yip, S. K. So, S. Beaupre, M. Mainville, P. A. Johnson, M. Leclerc, H. Chen, H. Peng, Y. Li and Y. Zou, *Adv. Mater.*, 2019, **31**, 1807577.
101 J. Yuan, Y. Zhang, L. Zhou, G. Zhang, H.-L. Yip, T.-K. Lau, X. Lu, C. Zhu, H. Peng, P. A. Johnson, M. Leclerc, Y. Cao, J. Ulanski, Y. Li and Y. Zou, *Joule*, 2019, **3**, 1140–1151.
102 J. Yuan, H. Zhang, R. Zhang, Y. Wang, J. Hou, M. Leclerc, X. Zhan, F. Huang, F. Gao, Y. Zou and Y. Li, *Chem*, 2020, **6**, 2147–2161.
103 G. Zhang, X. K. Chen, J. Xiao, P. C. Y. Chow, M. Ren, G. Kupgan, X. Jiao, C. C. S. Chan, X. Du, R. Xia, Z. Chen, J. Yuan, Y. Zhang, S. Zhang, Y. Liu, Y. Zou, H. Yan, K. S. Wong, V. Coropceanu, N. Li, C. J. Brabec, J. L. Bredas, H. L. Yip and Y. Cao, *Nat. Commun.*, 2020, **11**, 3943.
104 W. Zhu, A. P. Spencer, S. Mukherjee, J. M. Alzola, V. K. Sangwan, S. H. Amsterdam, S. M. Swick, L. O. Jones, M. C. Heiber, A. A. Herzing, G. Li, C. L. Stern, D. M. DeLongchamp, K. L. Kohlstedt, M. C. Hersam, G. C. Schatz, M. R. Wasielewski, L. X. Chen, A. Facchetti and T. J. Marks, *J. Am. Chem. Soc.*, 2020, **142**, 14532–14547.
105 Z. Zhou, W. Liu, G. Zhou, M. Zhang, D. Qian, J. Zhang, S. Chen, S. Xu, C. Yang, F. Gao, H. Zhu, F. Liu and X. Zhu, *Adv. Mater.*, 2020, **32**, 1906324.
106 W. Gao, H. Fu, Y. Li, F. Lin, R. Sun, Z. Wu, X. Wu, C. Zhong, J. Min, J. Luo, H. Y. Woo, Z. Zhu and A. K.-Y. Jen, *Adv. Energy Mater.*, 2021, **11**, 2003177.
107 Z. Jia, S. Qin, L. Meng, Q. Ma, I. Angunawela, J. Zhang, X. Li, Y. He, W. Lai, N. Li, H. Ade, C. J. Brabec and Y. Li, *Nat. Commun.*, 2021, **12**, 178.
108 S. Dong, T. Jia, K. Zhang, J. Jing and F. Huang, *Joule*, 2020, **4**, 2004–2016.
109 J. Wu, J. Lee, Y.-C. Chin, H. Yao, H. Cha, J. Luke, J. Hou, J.-S. Kim and J. R. Durrant, *Energy Environ. Sci.*, 2020, **13**, 2422–2430.
110 C. Zhang, J. Yuan, K. L. Chiu, H. Yin, W. Liu, G. Zheng, J. K. W. Ho, S. Huang, G. Yu, F. Gao, Y. Zou and S. K. So, *J. Mater. Chem. A*, 2020, **8**, 8566–8574.
111 Y. Cui, H. Yao, J. Zhang, T. Zhang, Y. Wang, L. Hong, K. Xian, B. Xu, S. Zhang, J. Peng, Z. Wei, F. Gao and J. Hou, *Nat. Commun.*, 2019, **10**, 2515.
112 Z. Luo, R. Ma, Z. Chen, Y. Xiao, G. Zhang, T. Liu, R. Sun, Q. Zhan, Y. Zou, C. Zhong, Y. Chen, H. Sun, G. Chai, K. Chen, X. Guo, J. Min, X. Lu, C. Yang and H. Yan, *Adv. Energy Mater.*, 2020, **10**, 2002649.
113 W. Shockley and H. J. Queisser, *J. Appl. Phys.*, 1961, **32**, 510–519.
114 Y. He and Y. Li, *Phys. Chem. Chem. Phys.*, 2011, **13**, 1970–1983.
115 R. Kerremans, C. Kaiser, W. Li, N. Zarrabi, P. Meredith and A. Armin, *Adv. Opt. Mater.*, 2020, **8**, 2000319.
116 Y. Firdaus, V. M. Le Corre, S. Karuthedath, W. Liu, A. Markina, W. Huang, S. Chattopadhyay, M. M. Nahid, M. I. Nugraha, Y. Lin, A. Seitkhan, A. Basu, W. Zhang, I. McCulloch, H. Ade, J. Labram, F. Laquai, D. Andrienko, L. J. A. Koster and T. D. Anthopoulos, *Nat. Commun.*, 2020, **11**, 5220.
117 H. Yao, Y. Cui, R. Yu, B. Gao, H. Zhang and J. Hou, *Angew. Chem., Int. Ed.*, 2017, **56**, 3045–3049.
118 Y. Lin, J. Wang, Z. G. Zhang, H. Bai, Y. Li, D. Zhu and X. Zhan, *Adv. Mater.*, 2015, **27**, 1170–1174.
119 W. Zhao, D. Qian, S. Zhang, S. Li, O. Inganas, F. Gao and J. Hou, *Adv. Mater.*, 2016, **28**, 4734–4739.
120 W. Li, K. H. Hendriks, W. S. Roelofs, Y. Kim, M. M. Wienk and R. A. Janssen, *Adv. Mater.*, 2013, **25**, 3182–3186.
121 Y. Jin, Z. Chen, M. Xiao, J. Peng, B. Fan, L. Ying, G. Zhang, X.-F. Jiang, Q. Yin, Z. Liang, F. Huang and Y. Cao, *Adv. Energy Mater.*, 2017, **7**, 1700944.
122 T. M. Clarke and J. R. Durrant, *Chem. Rev.*, 2010, **110**, 6736–6767.
123 B. Siegmund, M. T. Sajjad, J. Widmer, D. Ray, C. Koerner, M. Riede, K. Leo, I. D. Samuel and K. Vandewal, *Adv. Mater.*, 2017, **29**, 1604424.
124 Y. Lin, F. Zhao, S. K. K. Prasad, J. D. Chen, W. Cai, Q. Zhang, K. Chen, Y. Wu, W. Ma, F. Gao, J. X. Tang, C. Wang, W. You, J. M. Hodgkiss and X. Zhan, *Adv. Mater.*, 2018, **30**, 1706363.
125 S. Chandrabose, K. Chen, A. J. Barker, J. J. Sutton, S. K. K. Prasad, J. Zhu, J. Zhou, K. C. Gordon, Z. Xie, X. Zhan and J. M. Hodgkiss, *J. Am. Chem. Soc.*, 2019, **141**, 6922–6929.
126 L. Ma, S. Zhang, H. Yao, Y. Xu, J. Wang, Y. Zu and J. Hou, *ACS Appl. Mater. Interfaces*, 2020, **12**, 18777–18784.
127 M. Azzouzi, T. Kirchartz and J. Nelson, *Trends Chem.*, 2019, **1**, 49–62.
128 V. Coropceanu, X.-K. Chen, T. Wang, Z. Zheng and J.-L. Brédas, *Nat. Rev. Mater.*, 2019, **4**, 689–707.
129 X. Liu, B. P. Rand and S. R. Forrest, *Trends Chem.*, 2019, **1**, 815–829.

130 S. M. Menke, N. A. Ran, G. C. Bazan and R. H. Friend, *Joule*, 2018, **2**, 25–35.
131 K. Vandewal, K. Tvingstedt, A. Gadisa, O. Inganas and J. V. Manca, *Nat. Mater.*, 2009, **8**, 904–909.
132 J. Benduhn, K. Tvingstedt, F. Piersimoni, S. Ullbrich, Y. Fan, M. Tropiano, K. A. McGarry, O. Zeika, M. K. Riede, C. J. Douglas, S. Barlow, S. R. Marder, D. Neher, D. Spoltore and K. Vandewal, *Nat. Energy*, 2017, **2**, 17053.
133 D. C. Coffey, B. W. Larson, A. W. Hains, J. B. Whitaker, N. Kopidakis, O. V. Boltalina, S. H. Strauss and G. Rumbles, *J. Phys. Chem. C*, 2012, **116**, 8916–8923.
134 X. Liu, Y. Li, K. Ding and S. Forrest, *Phys. Rev. Appl.*, 2019, **11**, 024060.
135 R. A. Marcus, *J. Chem. Phys.*, 1965, **43**, 679–701.
136 C. P. Hsu, *Phys. Chem. Chem. Phys.*, 2020, **22**, 21630–21641.
137 T. Liu and A. Troisi, *J. Phys. Chem. C*, 2011, **115**, 2406–2415.
138 L. Zhu, Y. Yi and Z. Wei, *J. Phys. Chem. C*, 2018, **122**, 22309–22316.
139 A. Classen, C. L. Chochos, L. Lüer, V. G. Gregoriou, J. Wortmann, A. Osvet, K. Forberich, I. McCulloch, T. Heumüller and C. J. Brabec, *Nat. Energy*, 2020, **5**, 711–719.
140 C. Sun, S. Qin, R. Wang, S. Chen, F. Pan, B. Qiu, Z. Shang, L. Meng, C. Zhang, M. Xiao, C. Yang and Y. Li, *J. Am. Chem. Soc.*, 2020, **142**, 1465–1474.
141 F. D. Eisner, M. Azzouzi, Z. Fei, X. Hou, T. D. Anthopoulos, T. J. S. Dennis, M. Heeney and J. Nelson, *J. Am. Chem. Soc.*, 2019, **141**, 6362–6374.
142 D. Bartesaghi, C. Perez Idel, J. Kniepert, S. Roland, M. Turbiez, D. Neher and L. J. Koster, *Nat. Commun.*, 2015, **6**, 7083.
143 X. Du, T. Heumueller, W. Gruber, O. Almora, A. Classen, J. Qu, F. He, T. Unruh, N. Li and C. J. Brabec, *Adv. Mater.*, 2020, **32**, 1908305.
144 F. Gajdos, H. Oberhofer, M. Dupuis and J. Blumberger, *J. Phys. Chem. Lett.*, 2014, **5**, 2765–2766.
145 F. Hamada and A. Saeki, *ChemSusChem*, 2021, **14**, 1–8.
146 C. Liu, K. Huang, W.-T. Park, M. Li, T. Yang, X. Liu, L. Liang, T. Minari and Y.-Y. Noh, *Mater. Horiz.*, 2017, **4**, 608–618.
147 G. Kupgan, X.-K. Chen and J.-L. Brédas, *ACS Mater. Lett.*, 2019, **1**, 350–353.
148 S. Himmelberger and A. Salleo, *MRS Commun.*, 2015, **5**, 383–395.
149 M. Kim, S. U. Ryu, S. A. Park, K. Choi, T. Kim, D. Chung and T. Park, *Adv. Funct. Mater.*, 2020, **30**, 1904545.
150 J. Wang, J. Zhang, Y. Xiao, T. Xiao, R. Zhu, C. Yan, Y. Fu, G. Lu, X. Lu, S. R. Marder and X. Zhan, *J. Am. Chem. Soc.*, 2018, **140**, 9140–9147.
151 S. Dai, J. Zhou, S. Chandrabose, Y. Shi, G. Han, K. Chen, J. Xin, K. Liu, Z. Chen, Z. Xie, W. Ma, Y. Yi, L. Jiang, J. M. Hodgkiss and X. Zhan, *Adv. Mater.*, 2020, **32**, 2000645.
152 H. Lai, H. Chen, J. Zhou, J. Qu, P. Chao, T. Liu, X. Chang, N. Zheng, Z. Xie and F. He, *iScience*, 2019, **17**, 302–314.
153 G. Han, T. Hu and Y. Yi, *Adv. Mater.*, 2020, **32**, 2000975.
154 X. Du, Y. Yuan, L. Zhou, H. Lin, C. Zheng, J. Luo, Z. Chen, S. Tao and L. S. Liao, *Adv. Funct. Mater.*, 2020, **30**, 1909837.
155 B. T. Luppi, D. Majak, M. Gupta, E. Rivard and K. Shankar, *J. Mater. Chem. A*, 2019, **7**, 2445–2463.
156 M. K. Etherington, J. Wang, P. C. Y. Chow and N. C. Greenham, *Appl. Phys. Lett.*, 2014, **104**, 063304.
157 D. Veldman, S. C. J. Meskers and R. A. J. Janssen, *Adv. Funct. Mater.*, 2009, **19**, 1939–1948.
158 C. W. Schlenker, K. S. Chen, H. L. Yip, C. Z. Li, L. R. Bradshaw, S. T. Ochsenbein, F. Ding, X. S. Li, D. R. Gamelin, A. K.-Y. Jen and D. S. Ginger, *J. Am. Chem. Soc.*, 2012, **134**, 19661–19668.
159 A. Rao, P. C. Chow, S. Gelinas, C. W. Schlenker, C. Z. Li, H. L. Yip, A. K.-Y. Jen, D. S. Ginger and R. H. Friend, *Nature*, 2013, **500**, 435–439.
160 X. K. Chen, T. Wang and J. L. Brédas, *Adv. Energy Mater.*, 2017, **7**, 1602713.
161 Y. Jin, Y. Zhang, Y. Liu, J. Xue, W. Li, J. Qiao and F. Zhang, *Adv. Mater.*, 2019, **31**, 1900690.
162 S. Kappaun, C. Slugovc and E. J. List, *Int. J. Mol. Sci.*, 2008, **9**, 1527–1547.
163 S. Goswami, J. L. Hernandez, M. K. Gish, J. Wang, B. Kim, A. P. Laudari, S. Guha, J. M. Papanikolas, J. R. Reynolds and K. S. Schanze, *Chem. Mater.*, 2017, **29**, 8449–8461.
164 L. Yang, W. Gu, L. Lv, Y. Chen, Y. Yang, P. Ye, J. Wu, L. Hong, A. Peng and H. Huang, *Angew. Chem., Int. Ed.*, 2018, **57**, 1096–1102.
165 S. Liu, H. Zhang, Y. Li, J. Liu, L. Du, M. Chen, R. T. K. Kwok, J. W. Y. Lam, D. L. Phillips and B. Z. Tang, *Angew. Chem., Int. Ed.*, 2018, **57**, 15189–15193.
166 H. Uoyama, K. Goushi, K. Shizu, H. Nomura and C. Adachi, *Nature*, 2012, **492**, 234–238.
167 M. J. Leitl, V. A. Krylova, P. I. Djurovich, M. E. Thompson and H. Yersin, *J. Am. Chem. Soc.*, 2014, **136**, 16032–16038.
168 L. Qin, X. Liu, X. Zhang, J. Yu, L. Yang, F. Zhao, M. Huang, K. Wang, X. Wu, Y. Li, H. Chen, K. Wang, J. Xia, X. Lu, F. Gao, Y. Yi and H. Huang, *Angew. Chem., Int. Ed.*, 2020, **59**, 15043–15049.
169 D. Kim, *J. Phys. Chem. C*, 2015, **119**, 12690–12697.
170 J. Xue, Q. Liang, R. Wang, J. Hou, W. Li, Q. Peng, Z. Shuai and J. Qiao, *Adv. Mater.*, 2019, **31**, 1808242.
171 B. Watts, W. J. Belcher, L. Thomsen, H. Ade and P. C. Dastoor, *Macromolecules*, 2009, **42**, 8392–8397.
172 N. D. Treat, M. A. Brady, G. Smith, M. F. Toney, E. J. Kramer, C. J. Hawker and M. L. Chabinyc, *Adv. Energy Mater.*, 2011, **1**, 82–89.
173 L. Ye, B. A. Collins, X. Jiao, J. Zhao, H. Yan and H. Ade, *Adv. Energy Mater.*, 2018, **8**, 1703058.
174 L. Ye, H. Hu, M. Ghasemi, T. Wang, B. A. Collins, J. H. Kim, K. Jiang, J. H. Carpenter, H. Li, Z. Li, T. McAfee, J. Zhao, X. Chen, J. L. Y. Lai, T. Ma, J. L. Bredas, H. Yan and H. Ade, *Nat. Mater.*, 2018, **17**, 253–260.
175 F. Zhao, C. Wang and X. Zhan, *Adv. Energy Mater.*, 2018, **8**, 1703147.
176 P. J. Flory, *Principles of Polymer Chemistry*, Cornell University Press, 1953.

177 P. Knychała, K. Timachova, M. Banaszak and N. P. Balsara, *Macromolecules*, 2017, **50**, 3051–3065.
178 T. Nishi and T. Wang, *Macromolecules*, 1975, **8**, 909–915.
179 C. Clarke, A. Eisenberg, J. La Scala, M. Rafailovich, J. Sokolov, Z. Li, S. Qu, D. Nguyen, S. Schwarz and Y. Strzhemechny, *Macromolecules*, 1997, **30**, 4184–4188.
180 J. E. Mark, *Physical Properties of Polymers Handbook*, Springer, 2007.
181 T. Lindvig, M. L. Michelsen and G. M. Kontogeorgis, *Fluid Phase Equilib.*, 2002, **203**, 247–260.
182 M. Gao, Z. Liang, Y. Geng and L. Ye, *Chem. Commun.*, 2020, **56**, 12463–12478.
183 L. Ye, S. Zhang, W. Ma, B. Fan, X. Guo, Y. Huang, H. Ade and J. Hou, *Adv. Mater.*, 2012, **24**, 6335–6341.
184 Z. Li, K. Jiang, G. Yang, J. Y. Lai, T. Ma, J. Zhao, W. Ma and H. Yan, *Nat. Commun.*, 2016, **7**, 13094.
185 F. Zhao, S. Dai, Y. Wu, Q. Zhang, J. Wang, L. Jiang, Q. Ling, Z. Wei, W. Ma, W. You, C. Wang and X. Zhan, *Adv. Mater.*, 2017, **29**, 1700144.
186 T. Ma, K. Jiang, S. Chen, H. Hu, H. Lin, Z. Li, J. Zhao, Y. Liu, Y.-M. Chang, C.-C. Hsiao and H. Yan, *Adv. Energy Mater.*, 2015, **5**, 1501282.
187 H. Hu, K. Jiang, G. Yang, J. Liu, Z. Li, H. Lin, Y. Liu, J. Zhao, J. Zhang, F. Huang, Y. Qu, W. Ma and H. Yan, *J. Am. Chem. Soc.*, 2015, **137**, 14149–14157.
188 L. Ye, W. Zhao, S. Li, S. Mukherjee, J. H. Carpenter, O. Awartani, X. Jiao, J. Hou and H. Ade, *Adv. Energy Mater.*, 2017, **7**, 1602000.
189 S. Li, L. Ye, W. Zhao, H. Yan, B. Yang, D. Liu, W. Li, H. Ade and J. Hou, *J. Am. Chem. Soc.*, 2018, **140**, 7159–7167.
190 J. Wu, G. Li, J. Fang, X. Guo, L. Zhu, B. Guo, Y. Wang, G. Zhang, L. Arunagiri, F. Liu, H. Yan, M. Zhang and Y. Li, *Nat. Commun.*, 2020, **11**, 4612.
191 C. Yang, S. Zhang, J. Ren, M. Gao, P. Bi, L. Ye and J. Hou, *Energy Environ. Sci.*, 2020, **13**, 2864–2869.
192 J. H. Carpenter, A. Hunt and H. Ade, *J. Electron Spectrosc. Relat. Phenom.*, 2015, **200**, 2–14.
193 S. A. Gevorgyan, M. V. Madsen, B. Roth, M. Corazza, M. Hösel, R. R. Søndergaard, M. Jørgensen and F. C. Krebs, *Adv. Energy Mater.*, 2016, **6**, 1501208.
194 T. M. Clarke, C. Lungenschmied, J. Peet, N. Drolet, K. Sunahara, A. Furube and A. J. Mozer, *Adv. Energy Mater.*, 2013, **3**, 1473–1483.
195 W. R. Mateker and M. D. McGehee, *Adv. Mater.*, 2017, **29**, 1603940.
196 N. Li, J. D. Perea, T. Kassar, M. Richter, T. Heumueller, G. J. Matt, Y. Hou, N. S. Guldal, H. Chen, S. Chen, S. Langner, M. Berlinghof, T. Unruh and C. J. Brabec, *Nat. Commun.*, 2017, **8**, 14541.
197 X. Du, T. Heumueller, W. Gruber, A. Classen, T. Unruh, N. Li and C. J. Brabec, *Joule*, 2019, **3**, 215–226.
198 S. Li, L. Ye, W. Zhao, X. Liu, J. Zhu, H. Ade and J. Hou, *Adv. Mater.*, 2017, **29**, 1704051.
199 S. Li, L. Ye, W. Zhao, S. Zhang, H. Ade and J. Hou, *Adv. Energy Mater.*, 2017, **7**, 1700183.
200 Q. Yue, W. Liu and X. Zhu, *J. Am. Chem. Soc.*, 2020, **142**, 11613–11628.
201 L. Ma, S. Zhang, J. Wang, Y. Xu and J. Hou, *Chem. Commun.*, 2020, **56**, 14337–14352.
202 C. J. Brabec, A. Distler, X. Du, H. J. Egelhaaf, J. Hauch, T. Heumueller and N. Li, *Adv. Energy Mater.*, 2020, **10**, 2001864.
203 K. Kranthiraja and A. Saeki, *Adv. Funct. Mater.*, 2021, **31**, 2011168.
204 W. Sun, Y. Zheng, K. Yang, Q. Zhang, A. A. Shah, Z. Wu, Y. Sun, L. Feng, D. Chen and Z. Xiao, *Sci. Adv.*, 2019, **5**, eaay4275.